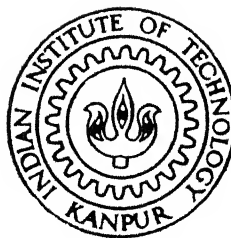


# Some Studies On Microstructural Characterization of Thermomechanically Treated Fe-28 at% Al Intermetallic Alloy

*by*

JOY MITTRA



MME

1996

M

MIT

SOM

Department of Materials and Metallurgical Engineering

INDIAN INSTITUTE OF TECHNOLOGY, KANPUR

July, 1996

**Some Studies On Microstructural Characterization of  
Thermomechanically Treated Fe-28 at% Al Intermetallic  
Alloy**

*By*  
Joy Mittra

UNDER THE GUIDANCE OF

Dr. S Bhargava  
Dr. S Sangal

*A Thesis  
Submitted in Partial Fulfillment of the Requirements*

FOR THE DEGREE OF  
**Master of Technology In Materials And Metallurgical  
Engineering**

*AT THE*  
INDIAN INSTITUTE OF TECHNOLOGY, KANPUR

DEPARTMENT OF MATERIALS AND METALLURGICAL ENGINEERING  
IIT, KANPUR

**JULY, 1996**

5 DEC :997  
CENTRAL LIBRARY  
U. S. MARINE  
124444



A124444

MME-1996-M-BHA-SOM

PRESENTED TO

SRI THE HONORABLE SHRI MAHAPATRA


AND

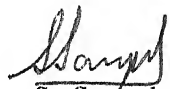
HIS FAMILIES



## CERTIFICATE

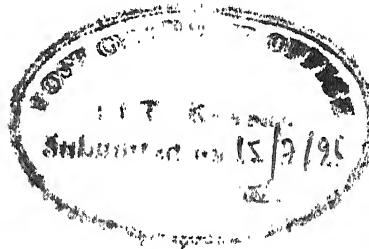
This is to certify that the work on "**Some Studies on Microstructural Characterization of Thermomechanically Treated Fe-28 at% Al Intermetallic Alloy**" has been carried out by Mr. Joy Mitra under our supervision and that it has not been submitted elsewhere for a degree.

  
S. Bhargava  
Professor

  
S. Sangal  
Assistant Professor

Department of Materials and Metallurgical Engineering  
Indian Institute of Technology, Kanpur

July, 1996



## ACKNOWLEDGMENT

I take this opportunity to acknowledge the help from the head of the department, Dr. Dubey and DPGC, Convenor for providing the facilities in time and granting me leave for three semesters.

I sincerely acknowledge the guidance and encouragement obtained from Dr. S. Bhargava and Dr. S. Sangal during this thesis work.

I am very grateful to Dr. Siddhartha Das and Mrs. D. Kanchanamala of IIT, Madras, for the immense help to complete some part of the work in their TEM. I am also grateful to Dr. Raju Ramanujan of Bhaba Atomic Research Center, Bombay, who provided necessary help to carry out sample preparation at that center and provided useful literature.

In this project work, valuable help was obtained from Mrs. M. Vijayalaksmi, Mr. P. Parameswaran, Dr. V. S. Raghunathan, Mr. C Balan and Mr. Thomas Paul of Physical Metallurgy Section, Indira Gandhi Center for Atomic Research, Kalpakkam. I sincerely acknowledge their help.

My sincere thanks to Dr. S. K. Ray and Dr. S. L. Mannan for their encouragement in carrying out the M.Tech project work and issuing leave in proper time.

Pravat, Sudipto, Liladhar, Mahesh and Barun of Kanpur, Aniruddha, Nagesh, Packiaraj Sreenivasan Nilangshu and Rama of Kalpakkam and Darshan Sathe of Tarapur and many other friends had their well wishes for accomplishment of my M.Tech. I am very thankful for the encouragement and help obtained from them.

Last but not least, I have my heartfelt gratitude to my parents, brother and God for their well wishes, inspiration and help to complete my project work.

## ABSTRACT

Study of the thermomechanically treated Fe-28 at% Al material samples were done by Transmission Electron Microscope. Characterization of the phases by TEM shows that ordered  $\text{DO}_3$  is formed in all the samples. The  $\text{DO}_3$  ordering is more prominent in case of samples rolled at 1000 °C than in the samples rolled at 800 °C and 500 °C. Effect of rolling on ordering is significant but the reason of ordering in this study is attributed to enhanced diffusion process, which occurred due to very low values of vacancy formation energy in this material.

## LIST OF FIGURES

- Figure-2.1: The Fe-Al phase diagram[9].
- Figure-2.2: Unit cell and antiphase vectors associated with the superlattice structures of Fe-Al system[12].
- Figure-2.2(a): DO<sub>3</sub> unit cell and its antiphase vectors.
- Figure-2.2(b): B2 unit cell and its antiphase vector.
- Figure-2.3: Temperature dependence of yield strength and operative slip planes for Fe-24.8 at% Al[19].
- Figure-2.4: Schematic illustration of possible perfect dislocations (a,b,f) and imperfect variants of superdislocations with APB trails (c,d,e) in DO<sub>3</sub> superlattice (a~e) and B2 superlattice[29]
- Figure-2.5: The dependence of the flow stress of Fe<sub>3</sub>Al on test temperature[19].
- Figure-2.6: The variation in the spacing of dislocations comprising a superdislocation with the long range order [4].
- Figure-2.7: Yield stress and hardness as a function of composition for AgMg, AuZn, CoAl, FeAl and NiAl deformed at room temperature[20].
- Figure-2.8: Temperature dependence of yield stress at different composition of iron aluminides[23].
- Figure-2.9: Stress-strain curves of FeAl and NiAl at room temperature[25].
- Figure-2.10: TEM morphologies of dislocations in Fe<sub>3</sub>Al alloy at various strain, (a) undeformed; (b) 1.5% strain; (c) 3.3% strain[31].
- Figure-2.11: NNNAPB are formed by imperfect dislocations moving in Fe<sub>3</sub>Al[32].
- Figure-2.12: Subgrain boundary structure obtained after annealing rolled Fe-28 at% Al 5 at% Cr for 1h at 700 °C showing (a) bright field image, (b)weak beam image and (c) darkfield image, of 1/2<100> dislocation and APB faults in subgrain walls[32].
- Figure-2.13(a):Schematic representation of local relaxation of dislocation in subgrain boundary. Firm lines before and dotted lines after relaxation[33].
- Figure-2.13(b):Schematic diagram showing dislocations in subgrain boundary of figure-2.12(b,c), near A, identifying Burgers vectors[32].
- Figure-2.14: Activation energies versus x in Fe<sub>1-x</sub>Al<sub>x</sub> [35].

- Figure-3.1: Schematic diagram of a dual jet polisher.
- Figure-3.2: Diagrammatic representation of a spot pattern. (Possible reciprocal cell edges along OA and OB.)[30].
- Figure-4.1: Morphology of superdislocations in  $\text{DO}_3$ ; RS1000, 50,000X.
- Figure-4.2: A region of RS1000 showing partially recovered structure; 25,000X.
- Figure-4.3: Diffraction pattern obtained from RS1000. This pattern is similar to the pattern of figure-4.17. Analysis is given in the figure-4.3(a).
- Figure-4.4: Closely placed superlattice dislocation indicating presence of ordered crystal structure in RS1000; 100,000X.
- Figure-4.5: Transmitted electron diffraction pattern showing streaks and doubly diffracted spots in RS1000.
- Figure-4.6: TEM morphology, showing the formation of APB by superdislocations, RS1000; 13,500X.
- Figure-4.7: The diffraction pattern from the region of figure-4.6. Stacking faults and doubly twinned faults are observed, RS1000.
- Figure-4.8: TEM morphology showing different types of dislocations and APB faults in the boundary walls where local relaxation of boundary wall has taken place in RS1000; 40,000X. [See figure-2.12(a)].
- Figure-4.9: Selected area diffraction (SAD) pattern near the region of figure-4.8 indicating  $\text{DO}_3$  structure.
- Figure-4.10: Deformation contour in RS1000; 60,000X.
- Figure-4.11: TEM morphology showing moving dislocations with an interdislocation spacing of 120 nm in the ordered  $\text{DO}_3$  superlattice. RS1000; 100,000X.
- Figure-4.12: SAD pattern from the region of figure 4.11.
- Figure-4.13: TEM morphology showing dislocations in RS1000; 3,900X.
- Figure-4.14: TEM morphology showing dislocations and slip bands in RS1000; 3,900X.
- Figure-4.15: Micrographs imaging the relaxation of dislocation at the subgrain boundary walls in RS1000; 10,500X.

- Figure-4.16: APB walls near the region of figure 4.15; 10,500X.
- Figure-4.17: SAD pattern from the region of figure-4.18 indicating existence of DO<sub>3</sub> phase in RS1000. Analysis is given in figure-4.17(a).
- Figure-4.18: TEM morphology showing small domain of DO<sub>3</sub> in RS1000; 10,000X.
- Figure-4.19: SAD pattern obtained in the region of figure-4.20 showing superimposition two patterns, indicating existence of DO<sub>3</sub> and B2 phases in RS1000.
- Figure-4.20: TEM morphology showing deformation contour which appears dark in the figure; 50,000X.
- Figure-4.21: SAD pattern obtained from the region of figure-4.22 showing coexistence of DO<sub>3</sub> and  $\alpha$  phase and faults in the matrix in RS1000.
- Figure-4.22: Transmission electron micrographs showing dark region of heavily dislocated area; 30,000X.
- Figure-4.23: TEM morphology showing existence of small foreign particles, which are elongated into needle shape due to heavy deformation in RS1000; 30,000X.
- Figure-4.24: Magnified view of one such needle. superlattice dislocations are observed around such particles; 150,000X.
- Figure-4.25: The micrographs showing dislocations which are revealed near deformation band because of suitable orientation in RS1000; 17,000X.
- Figure-4.26: SAD pattern, indicating existence of B2 and DO<sub>3</sub> and same as figure 4.19. Analysis of the pattern is given in figure 4.26(a).
- Figure-4.27: TEM morphology of RS800 showing deformation band; 28,000X.
- Figure-4.28: Transmission electron micrographs of RS800 revealing superdislocation and small embedded particles; 46,000X.
- Figure-4.29: SAD pattern obtained from RS800, whose reciprocal lattice can be compared to the pattern of either [001] zone axis of DO<sub>3</sub> or [001] zone axis of B2. Analysis is given in the figure 4.29(a).
- Figure-4.30: Micrograph showing the region from where the above pattern is obtained.

- Figure-4.31: SAD pattern, similar to that of figure 4.29 but where double diffraction of  $\{400\}$  position of  $\text{DO}_3$  (or  $\{200\}$  position of B2) is prominent. Analysis is given in the figure-4.31(a); RS800.
- Figure-4.32: TEM morphology showing the region of figure 4.31, where dislocations in this superstructure is revealed on the deformation band; 25,000X.
- Figure-4.33: Dark field images showing elongated domain boundary in RS800; 40,000X.
- Figure-4.34: Spots of uniform intensity is observed in this SAD pattern of RS800. Kikuchi lines are obtained due to thick region of the sample. Analysis is given in the figure-4.34(a).
- Figure-4.35: The micrograph showing the region from where the pattern of figure-4.34 is obtained; RS800; 22,100X.
- Figure-4.36: TEM morphology of RS500 showing the deformation contour, high density of dislocations makes some regions appear dark; 22,000X.
- Figure-4.37: SAD pattern obtained from the region of figure-4.36 is similar to figure-4.29.
- Figure-4.38: SAD pattern indicating the possibility of existing  $\text{DO}_3$  and B2 with a  $\langle 111 \rangle$  type zone axis. Analysis is given in the figure-4.38(a).
- Figure-4.39: TEM morphology of RS500, from where the pattern of figure-4.39 is obtained, showing network of superdislocations; 50,000X.
- Figure-4.40: SAD pattern, obtained near the region of figure-4.39 is similar to that of figure-4.38.
- Figure-4.41: Transmission electron micrograph showing the heavily dislocated region where recovery has not taken place; RS500; 120,000X.
- Figure-4.42: SAD pattern obtained near the region of figure-4.41 is similar to that of figure-4.31. Analysis is given in the figure-4.42(a).

Figure-4.3(a): RS1000; L=150 mm, 160 kV; Zone axis  $[\bar{2}33]$   $\text{DO}_3$ .

Figure-4.5(a): RS1000; L=230 mm, 100 kV; Zone axis  $[001]$   $\text{DO}_3$  /  $[001]$  B2.

Figure-4.7(a): RS1000; L=155 mm, 100 kV; Zone axis  $[\bar{1}11]$   $\text{DO}_3$  /  $[\bar{1}11]$  B2.

Figure-4.9(a): RS1000; L=150 mm, 160 kV; Zone axis  $[\bar{1}22]$   $\text{DO}_3$ .

Figure-4.12(a): RS1000; L=150 mm, 160 kV; Zone axis  $[\bar{1}13]$   $\text{DO}_3$  /  $[\bar{1}13]$  B2.

Figure-4.17(a):RS1000; L=150 mm, 160 kV; Zone axis  $[\bar{2}33]$   $\text{DO}_3$  and  $[\bar{1}11]$  disordered b.c.c.

Figure-4.19(a):RS1000; L=150 mm, 160 kV; Zone axis  $[011]$   $\text{DO}_3$  and  $[011]$  B2.

Figure-4.21(a):RS1000; L=150 mm, 160 kV; Zone axis  $[011]$   $\text{DO}_3$  and  $[012]$  disordered b.c.c.

Figure-4.26(a):RS1000; L=575 mm, 100 kV; Zone axis  $[011]$   $\text{DO}_3$  and  $[011]$  B2.

Figure-4.29(a):RS800; L=575 mm, 100 kV; Zone axis  $[001]$   $\text{DO}_3$  /  $[001]$  B2.

Figure-4.31(a):RS800; L=150 mm, 160 kV; Zone axis  $[001]$   $\text{DO}_3$  /  $[001]$  B2.

Figure-4.34(a):RS800; L=155 mm, 100 kV; Zone axis  $[001]$   $\text{DO}_3$  /  $[001]$  B2.

Figure-4.37(a):RS500; L=575 mm, 100 kV; Zone axis  $[001]$   $\text{DO}_3$  /  $[001]$  B2.

Figure-4.38(a):RS500; L=150 mm, 160 kV; Zone axis  $[\bar{1}11]$   $\text{DO}_3$  /  $[\bar{1}11]$  B2.

Figure-4.40(a):RS500; L=150 mm, 160 kV; Zone axis  $[\bar{1}11]$   $\text{DO}_3$  /  $[\bar{1}11]$  B2.

Figure-4.42(a):RS500; L=150 mm, 160 kV; Zone axis  $[001]$   $\text{DO}_3$  /  $[001]$  B2.



## LIST OF TABLES

- TABLE-4.1: Wavelength of electron beam at different accelerating voltages.
- TABLE-4.2: X-ray diffraction data of  $\text{Fe}_3\text{Al}(\text{DO}_3)$  [39].
- TABLE-4.3: X-ray diffraction data of  $\alpha$ (disordered b.c.c.) iron [39].
- TABLE-4.4: X-ray diffraction data of  $\text{FeAl}(\text{B2})$  [38].
- TABLE-4.3(a): Giving the analysis of Selected Area Diffraction pattern of figure-4.3(a).
- TABLE-4.5(a): Giving the analysis of Selected Area Diffraction pattern of figure-4.5(a).
- TABLE-4.7(a): Giving the analysis of Selected Area Diffraction pattern of figure-4.7(a).
- TABLE-4.9(a): Giving the analysis of Selected Area Diffraction pattern of figure-4.9(a).
- TABLE-4.12(a): Giving the analysis of Selected Area Diffraction pattern of figure-4.12(a).
- TABLE-4.17(a): Giving the analysis of Selected Area Diffraction pattern of figure-4.17(a).
- TABLE-4.19(a): Giving the analysis of Selected Area Diffraction pattern of figure-4.19(a).
- TABLE-4.21(a): Giving the analysis of Selected Area Diffraction pattern of figure-4.21(a).
- TABLE-4.26(a): Giving the analysis of Selected Area Diffraction pattern of figure-4.26(a).
- TABLE-4.29(a): Giving the analysis of Selected Area Diffraction pattern of figure-4.29(a).
- TABLE-4.31(a): Giving the analysis of Selected Area Diffraction pattern of figure-4.31(a).
- TABLE-4.34(a): Giving the analysis of Selected Area Diffraction pattern of figure-4.34(a).
- TABLE-4.37(a): Giving the analysis of Selected Area Diffraction pattern of figure-4.37(a).
- TABLE-4.38(a): Giving the analysis of Selected Area Diffraction pattern of figure-4.38(a).
- TABLE-4.40(a): Giving the analysis of Selected Area Diffraction pattern of figure-4.40(a).
- TABLE-4.42(a): Giving the analysis of Selected Area Diffraction pattern of figure-4.42(a).

# CONTENTS

<b>ABSTRACT.....</b>	<b>V</b>
<b>LIST OF FIGURES.....</b>	<b>VI</b>
<b>LIST OF TABLES .....</b>	<b>XI</b>
<b>1: INTRODUCTION.....</b>	<b>1</b>
<b>2: LITERATURE REVIEW.....</b>	<b>3</b>
2.1: Fe <sub>3</sub> Al IN IRON ALUMINIDES SYSTEM .....	3
2.2: ATOMISTIC STUDIES OF B2 AND DO <sub>3</sub> STRUCTURES .....	5
2.3: MECHANICAL PROPERTIES .....	8
2.3.1: <i>SLIP SYSTEM</i> .....	8
2.3.2: <i>DEFORMATION BEHAVIOR</i> .....	8
2.3.3: <i>CREEP</i> .....	17
2.4: RECRYSTALLIZATION AND ORDER-DISORDER TRANSFORMATION IN Fe <sub>3</sub> Al.....	20
2.5: APPLICATION OF IRON ALUMINIDES .....	24
<b>3: EXPERIMENTAL PROCEDURE .....</b>	<b>27</b>
3.1: MATERIAL.....	27
3.2: THIN FOIL PREPARATION .....	27
3.3: MICROSTRUCTURAL ANALYSIS BY THE TRANSMISSION ELECTRON MICROSCOPY: ....	28
<b>4: RESULTS AND DISCUSSION.....</b>	<b>33</b>
<b>5: CONCLUSION.....</b>	<b>60</b>
<b>REFERENCES .....</b>	<b>61</b>

## INTRODUCTION

Body centered cubic based compounds with B2 and DO<sub>3</sub> structures have drawn considerable attention as candidates of high temperature structural materials. In this category iron aluminides are well known for their excellent resistance to high temperature sulfidizing and oxidizing environments. Among the various known iron aluminides Fe<sub>3</sub>Al compound has further importance because of their high specific strength, low density, electric and magnetic properties [1]. The widespread use of this material, however, has been restricted because of rapid drop of strength above ~500 °C and poor ductility at room temperature [2,3].

It has been suggested that, the rapid drop of strength above 500 °C is mainly affected by two factors, the transition of ordered DO<sub>3</sub> phase to B2 phase[4] and change in the order parameter of the DO<sub>3</sub> phase[5]. The DO<sub>3</sub>-B2 phase transition and the change of DO<sub>3</sub> ordering are influenced by the activation of superdislocations and the antiphase boundary(APB) energy.

The major reason for the low ductility of iron aluminides is the humidity induced hydrogen embrittlement. This was first identified by Liu et al[6] and substantiated by subsequent workers [7]. It is thought that aluminium atoms, which are freshly exposed during a tensile test, are oxidized by water vapor contained in the surrounding air. The oxidation is accompanied by a release of atomic hydrogen, which in turn causes hydrogen embrittlement.

After the pioneer work of Guttman [8], it is known that the order-disorder transition in the Fe<sub>3</sub>Al intermetallic compound is higher order phase transition. Since then many works have been done to understand the phase transition in the miscibility gap and as well as at other region of Fe-Al system. In most of the past experiments for studying phase transformation, equilibrium condition is followed with little or no consideration of kinetics.

The present study aims to understand ordering mechanism in  $\text{Fe}_3\text{Al}$  intermetallic compound due to deformation and considerably fast cooling rate, what is air cooling in the present study. To study the phase transition, transmission electron microscopic observation was done on heavily deformed, air cooled samples, which were available as thin strips. The micro-mechanism of phase transition is put forward with the help of present observation, in agreement with the earlier research works.

## LITERATURE REVIEW

### 2.1: *Fe<sub>3</sub>Al* IN IRON ALUMINIDES SYSTEM

The Fe<sub>3</sub>Al intermetallic compound has three different stable crystal structure in the solid state and these can be observed at three different temperature ranges. In the Fe-Al equilibrium diagram [figure-2.1], ordered DO<sub>3</sub> structure can be found over a narrow compositional range, near Fe<sub>3</sub>Al stoichiometry. DO<sub>3</sub> structure is stable up to 552 °C and it undergoes a phase transformation to B2 structure. B2 is stable up to around 800 °C and transforms into  $\alpha$ (disorder BCC) above that temperature. The  $\alpha$  phase is stable up to melting point of the alloy[9].

In the Fe-Al system both the first order and higher order phase transitions exist.  $\alpha$ , B2 and DO<sub>3</sub> are based on BCC crystal structure. As these phases are closely related in comparison to the crystal structure and lattice parameter, higher order phase transition is expected among them. In Fe-Al system disordered  $\alpha$ (Im3m) is the most symmetric phase. The  $\alpha$ -B2 phase transition is higher order phase transition. Therefore, symmetry is lost on the change to FeAl (Pm3m) [10]. The symmetry which is lost is  $\frac{1}{2}a<111>$  translation, which is nothing but the long range order parameter of B2 structure.

The B2-DO<sub>3</sub> equilibrium transition is also higher order phase transition. Both the  $\alpha$ -B2 and B2-DO<sub>3</sub> higher order phase transition takes place by continuous ordering[10]. The B2-DO<sub>3</sub> transition accompanies a loss in symmetry element of the parent crystal such as  $\frac{1}{2}a<100>$ .

The  $\alpha$ -B2 phase transition is fast and difficult to suppress by fast cooling. In case of quenching from high temperature ( $\alpha$  phase field)  $\alpha$ -B2 continuous ordering takes place leading to inhomogeneously dispersed small regions of B2(~200 Å

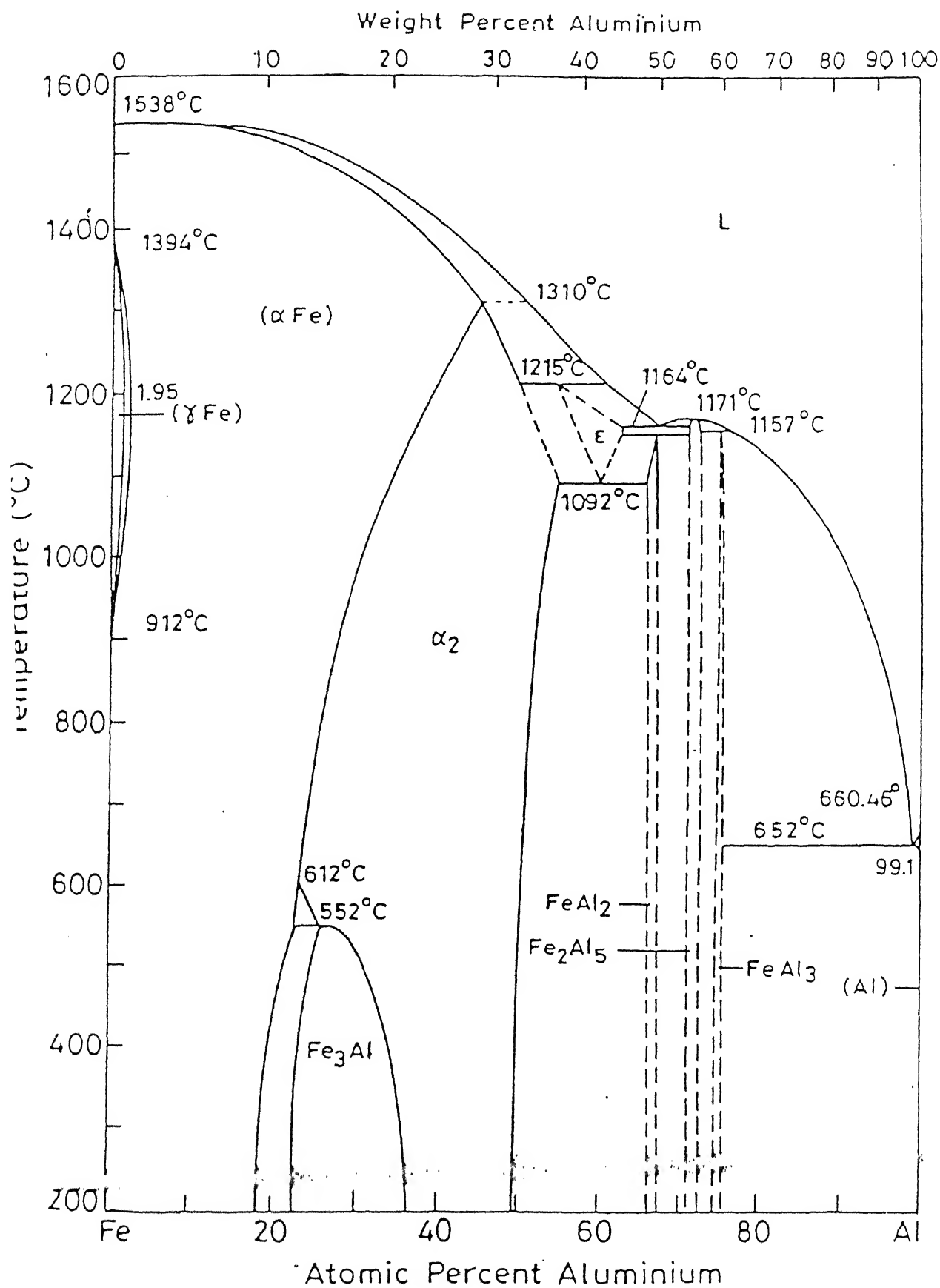


Figure-2.1: The Fe-Al phase diagram[9].

diameter) in the parent matrix. In comparison to  $\alpha$ -B2 transformation B2-DO<sub>3</sub> phase transformation is sluggish and can be suppressed by fast quenching [10,11].

## 2.2: ATOMISTIC STUDIES OF B2 AND DO<sub>3</sub> STRUCTURES

The unit cell and two types of antiphase vectors, given by Marcinkowski and Brown are illustrated in figure-2.2. Both the B2 and DO<sub>3</sub> superlattices are based on BCC crystal structures. In FeAl(B2) iron atoms occupy 'III' sites and Al atom occupies both 'II' and 'I' positions. Whereas in DO<sub>3</sub> structure iron atoms occupy 'III' positions and Al atoms occupy either 'II' or 'I' positions [12].

As it can be seen in figure-2.2(a), in case of DO<sub>3</sub>, lattice translation vector along  $\langle 111 \rangle$  is  $2a\langle 111 \rangle$ . So in case of DO<sub>3</sub> two types of APB's can be formed. One is by displacement of  $\frac{1}{2}a\langle 111 \rangle$  and another one is by displacement of  $a\langle 111 \rangle$ . But crystal structurewise  $\langle 001 \rangle$  is equivalent to the  $\langle 111 \rangle$  as the sites remain unchanged in DO<sub>3</sub> structure[13].

From the figure-2.2(b) it is clear that only one type of Antiphase boundary(APB) can exist in B2 structure. This APB in B2 FeAl is characterized by a displacement of  $\frac{1}{2}a\langle 111 \rangle$ , which can take place on its possible slip planes of  $\{100\}$  and  $\{112\}$ . Atomistically calculated  $\gamma$ -surface for the (110) plane in B2 structure indicates that only APB's are involved in dissociation of superlattice dislocations. This same principle is applicable to DO<sub>3</sub> structure also.

On the basis of crystal symmetry and restoring force calculation it is found that[14]  $\frac{1}{2}a\langle 111 \rangle$  APB's in B2 structure and  $\frac{1}{2}a\langle 111 \rangle$  and  $a\langle 100 \rangle$  in DO<sub>3</sub> structure are always stable. So, considering elastic energy of dislocation dissociation, the dislocation parallel to  $\langle 111 \rangle$  in the above two structure can be dissociated in the following two ways[15,16].

i] In the B2 structure

$$a\langle 111 \rangle = \frac{1}{2}a\langle 111 \rangle \times 2$$

...

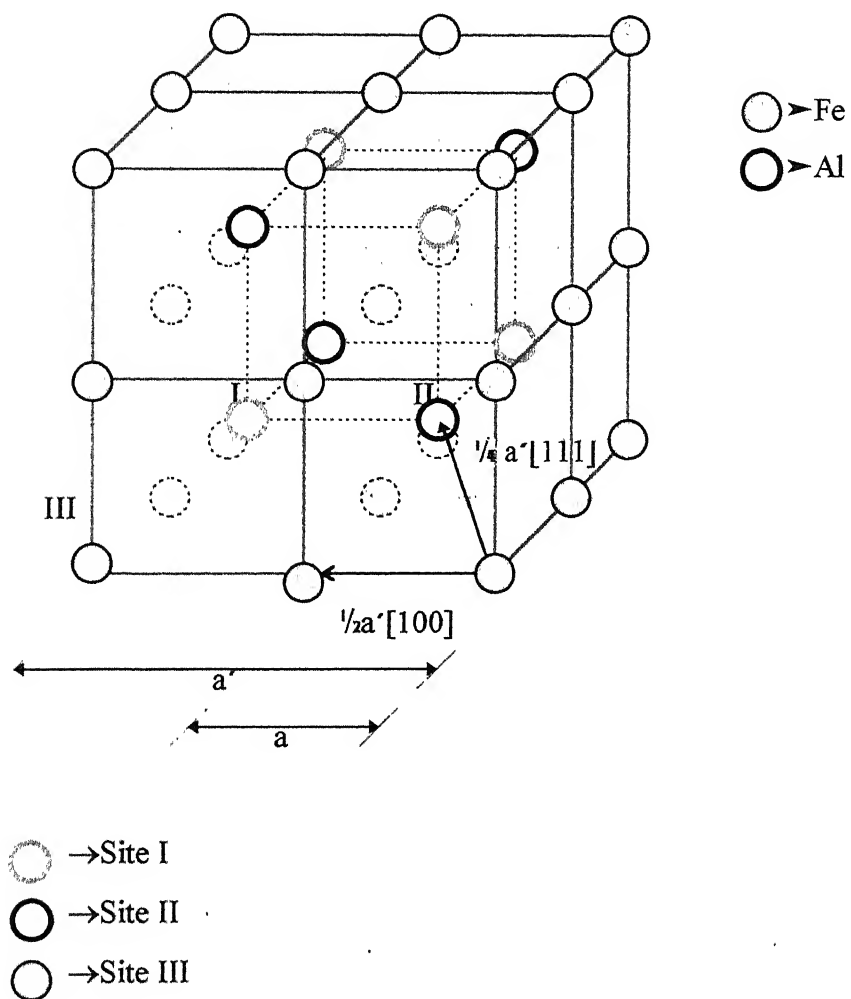


Figure-2.2: Unit cell and antiphase vectors associated with the superlattice structures of Fe-Al system[12].



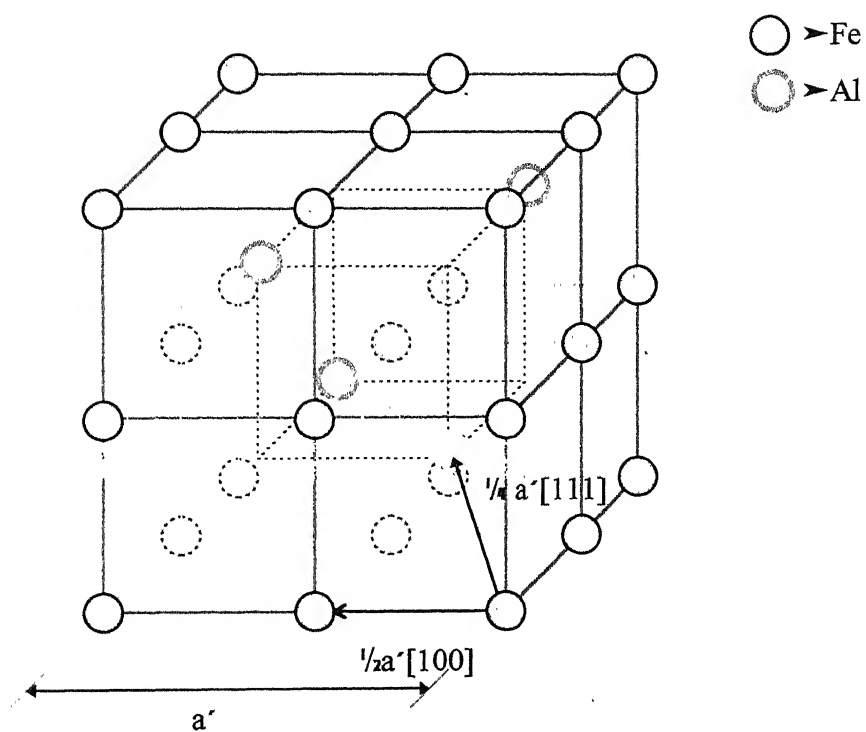


Figure-2.2(a): DO<sub>3</sub> unit cell and its antiphase vectors.

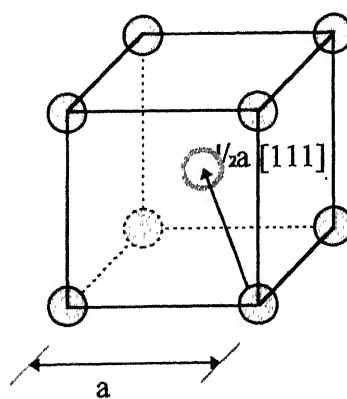


Figure-2.2(b): B2 unit cell and its antiphase vector.

ii] In the DO<sub>3</sub> structure

$$a'\langle 111 \rangle = \frac{1}{2}a\langle 111 \rangle \times 4$$

...

2.2

## **2.3: MECHANICAL PROPERTIES**

### **2.3.1: SLIP SYSTEM**

The favorable slip directions in B2 superstructure are either  $\langle 111 \rangle$  or  $\langle 001 \rangle$ . A transition of slip direction from  $\langle 111 \rangle$  to  $\langle 001 \rangle$  appears above  $0.4 T_m$  in ordered FeAl[17]. This phenomenon can be interpreted by the difference in critical resolved shear stress, which is function of temperature. According to Mendiratta et al[17], the temperature at which this change in slip direction occurs, increases with increasing of the off-stoichiometric Fe.

In DO<sub>3</sub> ordered Fe<sub>3</sub>Al most preferred slip direction is  $\langle 111 \rangle$ . In the  $\langle 111 \rangle$  direction both the  $\{110\}$  and  $\{112\}$  type slip planes can be activated. The choice of the slip plane is temperature dependent[18]. Below about 500 °C  $\{110\}$  type slip planes are preferred, whereas, above 500 °C  $\{112\}$  $\langle 111 \rangle$  slip systems are preferable. At high temperature, noncrystallographic slip systems are also observed to take part in deformation process in this material[19] [figure-2.3].

### **2.3.2: DEFORMATION BEHAVIOR**

The high yield stress in the Fe-Al system is attributed to the number of factors, namely composition, temperature and alloying elements. Micromechanismwise, these factors determine crystal structure, slip system and dislocation movement in the alloy. Above 26 at% Al stacking fault energy of the  $\langle 111 \rangle$  type fault vector increases rapidly enhancing the deformation process to be controlled by superlattice dislocation. Mendiratta et al[22] has shown the type of dislocation, that takes part in deformation, depends on stoichiometry of the system. A pictorial description of the dislocations, involved in the deformation process in B2 and DO<sub>3</sub> structure, are shown in the figure-2.4. There (a) and (b) are perfect superlattice dislocations in DO<sub>3</sub> and (f) is the perfect superlattice dislocation in B2 ordered structure. The ambient temperature deformation

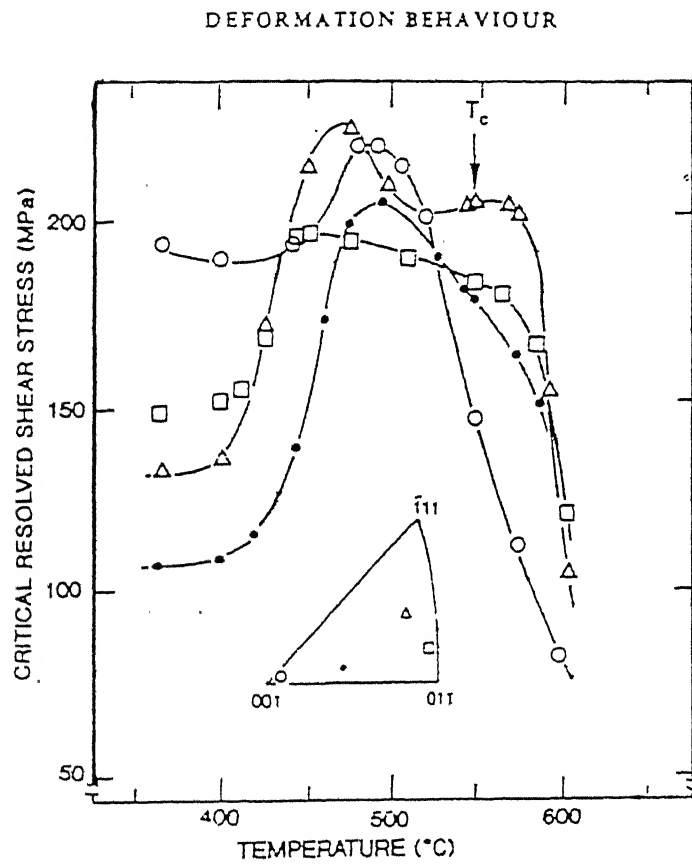
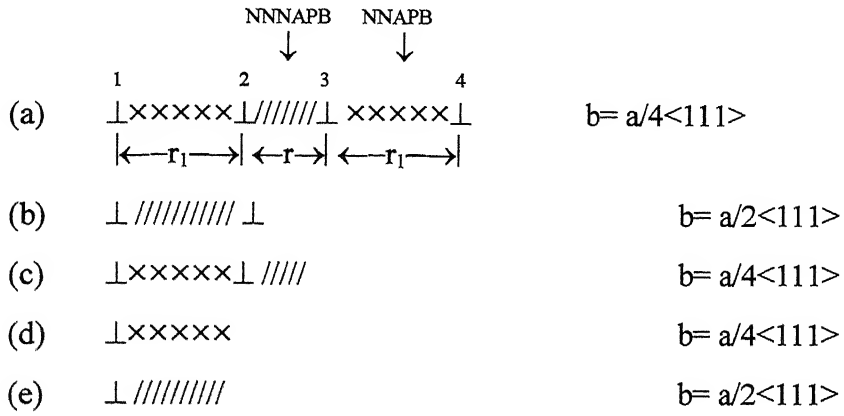


Figure-2.3: Temperature dependence of yield strength and operative slip planes for Fe-24.8 at% Al[19].

[DO<sub>3</sub>]



[B2]



Figure-2.4: Schematic illustration of possible perfect dislocations (a,b,f) and imperfect variants of superdislocations with APB trails (c,d,e) in DO<sub>3</sub> superlattice (a~e) and B2 superlattice[29].

of the alloy containing Al below 25 % is by ordinary dislocation of type (e) and (g). As the Al in the alloy is increased, the two component (b) or (f) type superlattice dislocations carry out the deformation process.

Degree of ordering in Fe<sub>3</sub>Al alloy has strong influence on the flow stress. A peak is observed in flow stress and in hardness at an intermediate ordering [figure-2.5]. To explain the peak in the flow stress, Sumino[41] proposed a theory based on dislocation behavior in the crystal. It says that, the stress field of an edge dislocation can induce the alignment of an short range order. In this case, long range order can restrict the development of stress-oriented short range order, so that a maximum in the dislocation locking force is to be anticipated at the critical temperature of ordering (T<sub>c</sub>). Stoloff and Davies[4] reported that, the mechanism suggested by Sumino is not applicable to Fe<sub>3</sub>Al as no discontinuity in the flow stress is observed at T<sub>c</sub> in this homogeneously ordered superlattice structure(DO<sub>3</sub>). As mentioned in the section-2.2 of this thesis and can be seen in the figure-2.4, perfect superdislocation consists of unit dislocations connected by a strip of APB. Energy of the APB, which is proportional to the ordering energy E<sub>OR</sub>, depends on the degree of long range order(LRO), S, through the relation,

$$E_{OR} = S^2 E_{OR}^{(s=1)} \quad \dots \quad 2.3$$

Where, the LRO parameter, S is defined as,

$$S = \left[ \frac{F(A,a) - F(a)}{1 - F(A)} \right] = \left[ \frac{F(B,b) - F(b)}{1 - F(B)} \right] \quad \dots \quad 2.4$$

Here, F(A,a) is the fraction of 'A' atoms on the 'A' sublattice and F(A) is the atom fraction in the A-B binary alloy system.

When S is low (say S=0.1), the ordinary dislocations which are constituent of superdislocation, can move independently. The APB trails left behind by the movement of ordinary dislocation are having wrong bonds and therefore responsible for hardening at low value of 'S'. When superdislocation glides in the perfectly ordered crystal it leaves no APB trails. So, a drop in flow stress is to be expected when large proportion of superdislocations are able to glide in pairs. Therefore, Stoloff and Davies[4] suggested a peak in the flow stress in an intermediate degree of ordering. With the help



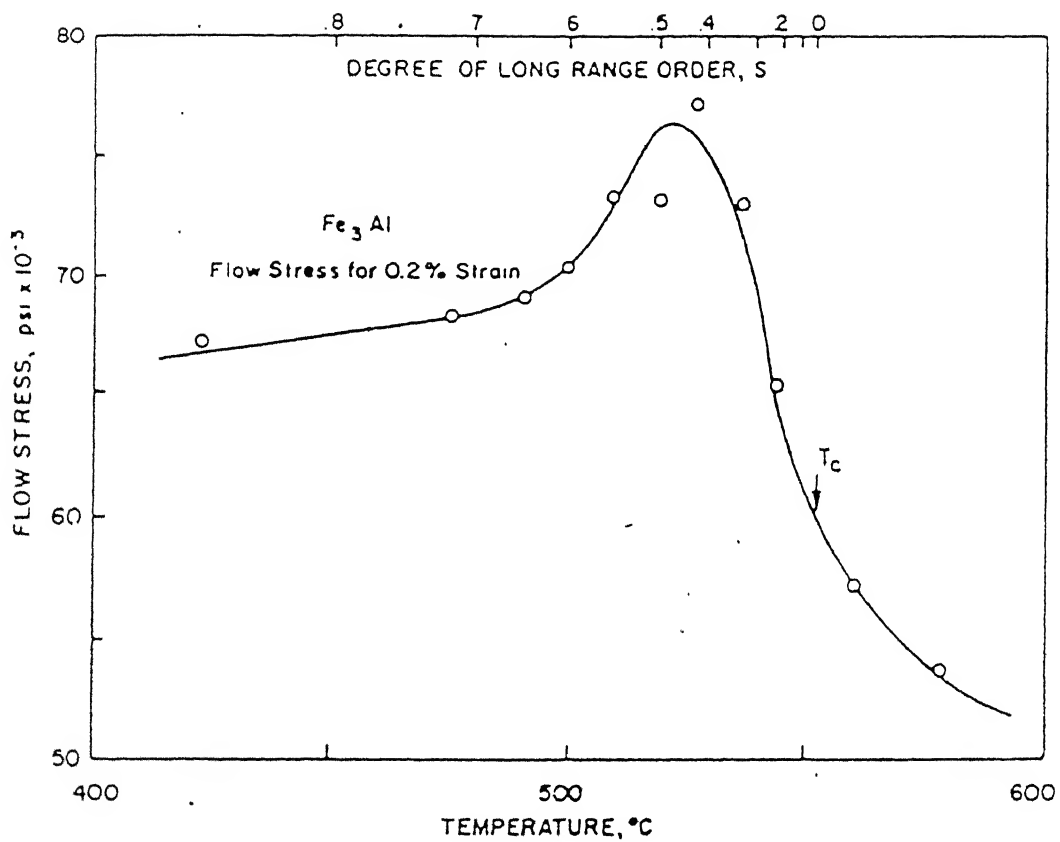


Figure-2.5: The dependence of the flow stress of  $\text{Fe}_3\text{Al}$  on test temperature[19].

of isotropic elasticity theory the calculated spacing,  $r$  [see figure-2.4], of a superdislocation can be given as ,

$$r = \frac{a_0^2 \sqrt{2Gb^2}}{2\pi k T_c S^2} \left[ \sin^2 \theta + \frac{\cos^2 \theta}{1 - \nu} \right] \quad \dots \quad 2.5$$

Where,  $a_0$  = the lattice parameter of B2;

$G$  = shear modulus;

$k$  = Boltzmann constant;

$T_c$  = critical temperature for ordering;

$\nu$  = Poisson ratio;

$\theta = 90^\circ$  for screw dislocation and  $0^\circ$  for edge dislocation.

Graphical representation of the equation-2.5 is shown in the figure-2.6. The  $DO_3$  type of order is decided by the next nearest neighbor interaction, while the nearest neighbor interaction decides B2 ordering, which does not change in disordering the  $DO_3$  lattice. Thus on decreasing the  $DO_3$  type of order, the superdislocations may be expected to split into two other superdislocations, connected by nearest neighbor antiphase boundary (NNAPB). Therefore, the main effect of changing the  $DO_3$  order is to change the spacing between dislocation 2 and 3 [figure-2.4], which are connected by the next nearest neighbor antiphase boundary (NNNAPB).

If a particular slip mode is considered, the flow stress is found to be strong function of composition in case of FeAl (B2) alloys. Effect of composition on yield stress and hardness of various intermetallic compounds are given in the figure-2.7[20]. Strength of FeAl decreases gradually with increase in iron content, away from stoichiometry [21]. At higher temperature ( $>0.6 T_m$ ) deformation is mainly controlled by the diffusion. So the strength of FeAl (Ordered) decreases rapidly. Therefore strength can be improved by suppressing diffusion.

A rapid drop in yield strength due to increase in Al content is very prominent in this system as shown in figure-2.8[23]. The higher strength at 24 at% Al is believed to be due to age hardening effect caused by  $\alpha$  precipitates in the  $DO_3$  matrix. In the composition range of 28-30 at% Al only  $DO_3$  structure exist, showing no such age

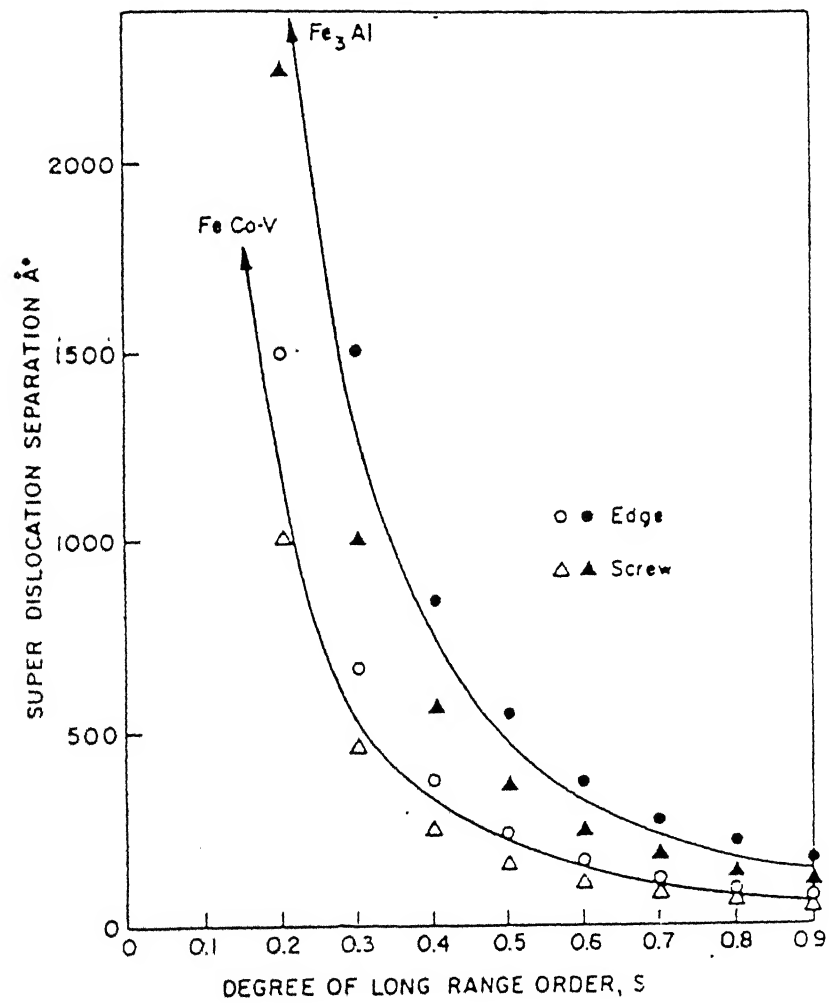


Figure-2.6: The variation in the spacing of dislocations comprising a superdislocation with the long range order [4].



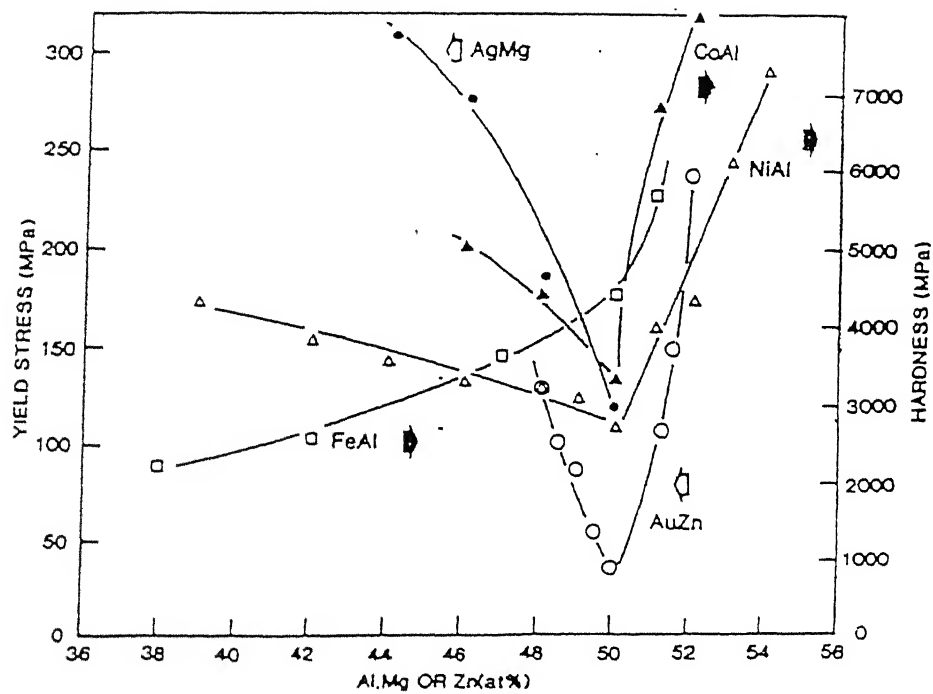


Figure-2.7: Yield stress and hardness as a function of composition for AgMg, AuZn, CoAl, FeAl and NiAl deformed at room temperature[20].

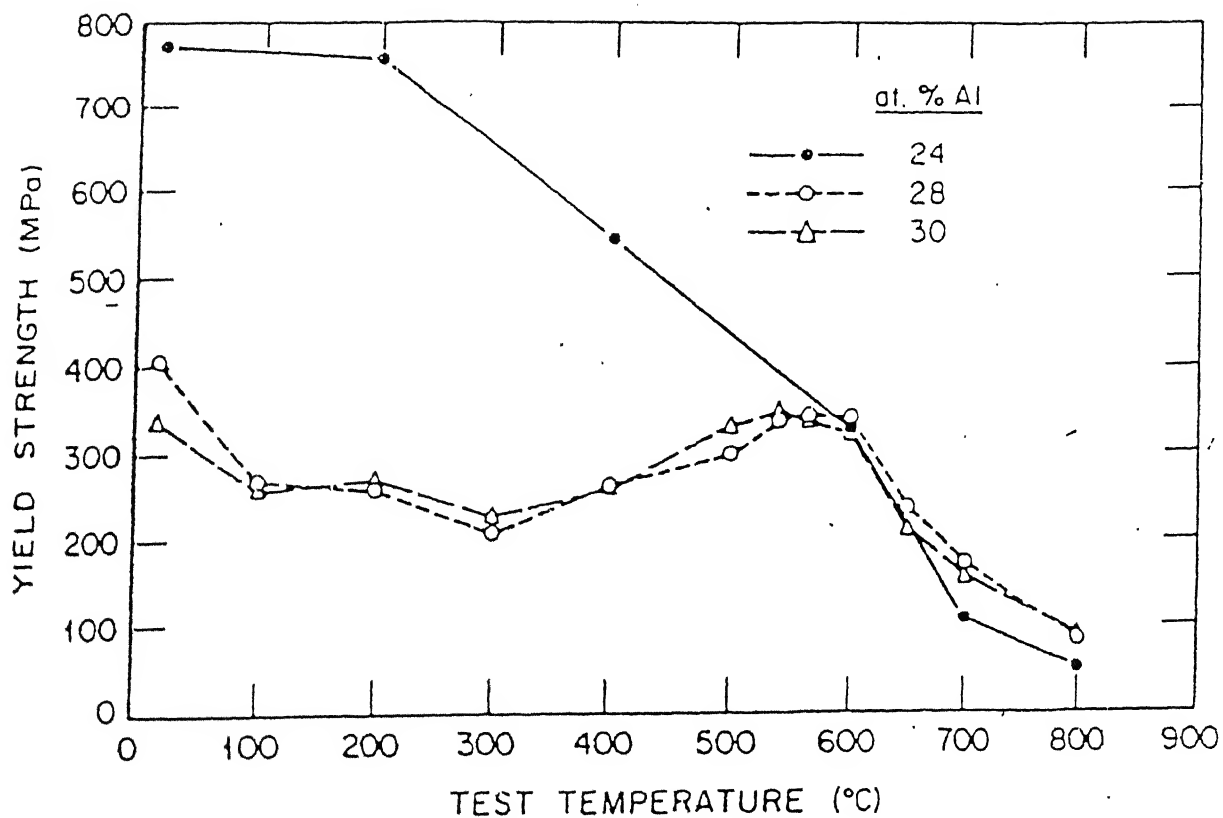


Figure-2.8: Temperature dependence of yield stress at different composition of iron aluminides[23].

hardening effect and therefore uniformity in the yield strength over a temperature range is observed.

Apart from thermomechanical treatment alone, the synergistic effect of various alloying elements and thermomechanical treatment is the present trend to improve the properties of Fe-Al based alloys. Cr addition [24] in the iron aluminides system is beneficial in the ductility point of view. It gives the adequate ductility at room temperature as well as considerable amount of strength at high temperature. This type of improvement in strength is attributed to improvement of cleavage strength such that fracture strength for transgranular fracture becomes comparable to that for intergranular fracture.

Similar to  $\text{Ni}_3\text{Al}$  system, B doping in the iron aluminides improves the room temperature ductility. The figure-2.9[25] indicates considerable amount of increase in ductility in both Ni-Al and Fe-Al system. It is believed that easy transmission of dislocation through grain boundary caused by B doping helps to avoid brittleness of the grain boundary[26]. The excess amount of B in these system segregates to the grain boundaries and strengthen it so that it can withstand stresses caused by planar array of dislocations.

### 2.3.3: CREEP

Two opposite processes may happen during high temperature deformation of  $\text{Fe}_3\text{Al}$  and Fe-Al based alloys. The first is strain induced disordering and the second is a opposing recovery process. This recovery process is observed during creep and this causes an increase in the degree of order[31]. The strain induced disordering process is evident from the dislocation configuration, obtained from the specimen, deformed at different strains at room temperature[31]. Figure-2.10(a) shows the four-fold superdislocations for the undeformed specimen which has  $\text{DO}_3$  structure. Figure-2.10(b) proves the occurrence of two-fold superdislocations for the specimens deformed to a strain of 1.5%. As the deformation strain increases to 3.3% [figure-2.10(c)] uncoupled dislocation appears. In the same specimen observation of slip bands and APB images indicate that the dislocation degeneration may increase the possibility of cross slip. The

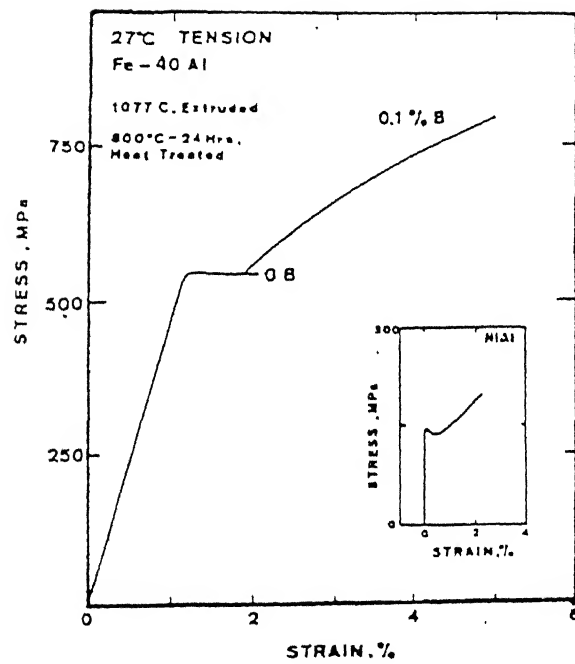


Figure-2.9: Stress-strain curves of FeAl and NiAl at room temperature[25].

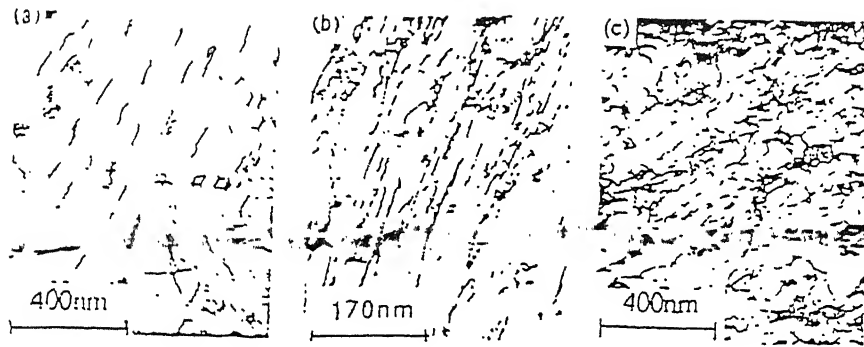


Figure-2.10: TEM morphologies of dislocations in  $\text{Fe}_3\text{Al}$  alloy at various strain, (a) undeformed; (b) 1.5% strain; (c) 3.3% strain[31].

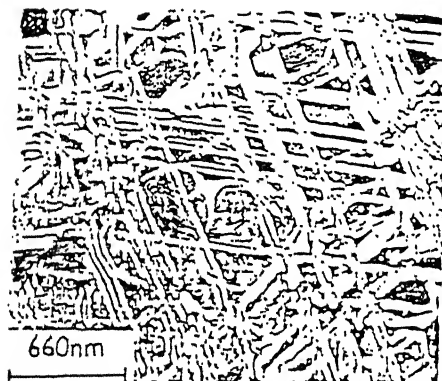


Figure-2.11: NNNAPB are formed by imperfect dislocations moving in  $\text{Fe}_3\text{Al}$ [32].

APB image [figure-2.11] obtained from the samples deformed at high temperature, using the  $\{111\}$  the superlattice spot for  $\text{Fe}_3\text{Al}$  binary alloy is straight. This indicates the absence of strain in the lattice, so that main four-fold superdislocation of  $\text{DO}_3$  are present. The splitting of four-fold superdislocation into two-fold is also observed by many other workers[4,32] and discussed in section-2.3.2 of this thesis.

The creep strength of intermetallic compound depends on the crystal orientation. In  $\text{FeAl}$ , creep is controlled by the viscous glide motion of the dislocations. At high temperature tangled ordinary  $\langle 001 \rangle$  dislocation (without subgrain formation) are found. As these types of dislocations are activated at high temperature the high APB energy ( $169 \text{ mJ/m}^2$ ) does not directly play an important role. This suggests that dislocation climb controls the creep in  $\text{FeAl}$  [27]. Therefore alloying addition is done to control dislocation motion at higher temperature. According to Mckamey[28], creep properties of  $\text{Fe}_3\text{Al}$  can be improved by adding Mo and B. Such addition improves rupture life to 57.4 hr. from 1.6 hr., in case of  $\text{Fe}_3\text{Al}$ , when tested at  $593^\circ\text{C}$  with a stress level of 207 MPa.

#### **2.4: RECRYSTALLIZATION AND ORDER-DISORDER TRANSFORMATION IN $\text{Fe}_3\text{Al}$**

The photographs in the figure-2.12 show the details of the subgrain boundary structure of Fe-28 at% Al-5% Cr alloy annealed at  $700^\circ\text{C}$  for 1 hr after rolling, followed by 15 hr at  $500^\circ\text{C}$  to establish a high degree of B2 and  $\text{DO}_3$  order[32]. Figure-2.12(a) shows array of dislocations which can be rendered invisible by imaging using 400 type diffraction vectors (corresponding to  $\text{DO}_3$  unit cell) and which are all visible when using 220g vector for imaging. The Burgers vector of the dislocations present are thus identified as  $[100]$  and  $[010]$ . Analysis of the line directions of the dislocations shows that they have near screw orientation. The details are clearly revealed in the figure 2.12(b) and (c) where the fine structure of dislocation interaction can be revealed. The dislocation arrangement in the recovery state, observed under TEM is first explained by Hirth and is similar to the study of Morris et al[32]. Figure-2.12(b) shows that a local relaxation of boundary dislocation has occurred after reaction with an oblique lattice dislocation and the pictorial representation can be given in the figure-2.13(a)[33]. Hirth pointed out that, before relaxation it is the situation

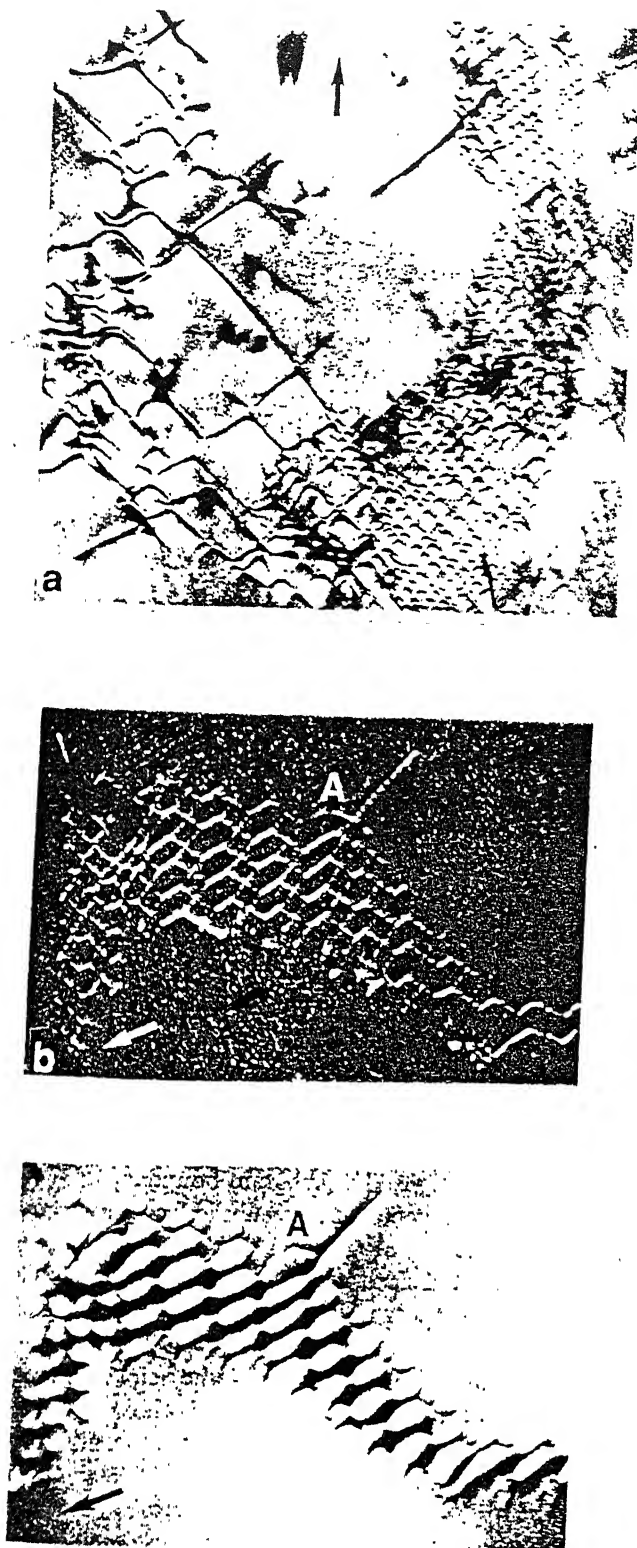


Figure-2.12: Subgrain boundary structure obtained after annealing rolled Fe-28 at% Al 5 at% Cr for 1h at 700 °C showing (a) bright field image, (b) weak beam image and (c) darkfield image, of  $1/2\langle 100 \rangle$  dislocation and APB faults in subgrain walls[32].

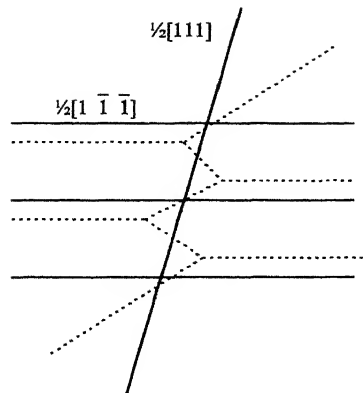


Figure-2.13(a): Schematic representation of local relaxation of dislocation in subgrain boundary. Firm lines before and dotted lines after relaxation[33].

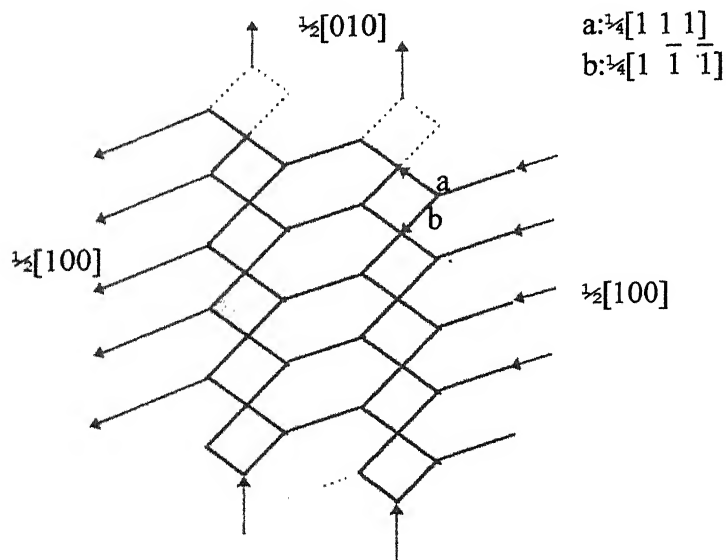


Figure-2.13(b): Schematic diagram showing dislocations in subgrain boundary of figure-2.12(b,c), near A, identifying Burgers vectors[32].



where a  $\frac{1}{2}[111]$  dislocation in molybdenum is entering a  $\frac{1}{2}[1\bar{1}\bar{1}]$  tilt wall and is represented by the firm line. Extension of this idea to the result of figure-2.12(b) can be seen in the figure-2.13(b). In this case the walls are composed of dislocations of Burgers vector  $[100]$  connected by dislocations in a diamond lattice arrangement of Burgers vector  $\frac{1}{4}[111]$  and  $\frac{1}{4}[1\bar{1}\bar{1}]$ . The magnitude of the Burgers vector is established in the following way. At first, the APB fault is distinguished in the figure-2.12(c) using a 200 g vector and hence the fault contained by the dislocations is a fault typical of the B2 ordering, produced by a  $\frac{1}{4}\langle 111 \rangle$  shear displacement. The microstructures of the figure-2.12 are confirmed to be produced during the high temperature recrystallization at 700 °C, with essentially no influence of the B2 ordering treatment[32].

When the materials containing this subgrain boundaries and their characteristic mixed Burgers vector dislocations are deformed, it is clear that mobile dislocations of type  $\langle 111 \rangle$ , that characterize room temperature deformation have difficulty in traversing the subgrain boundaries and do so with the accumulation of jogs. The consequence of this is that, the stress required is high and also, since the subgrain boundaries are not destroyed, deformation remain uniform and homogeneous.

Thermodynamically, feasibility of  $\alpha$  to  $\text{DO}_3$  was first considered by Allen and Cahn [10], which supported the result of Oki et al[5,10]. Oki et al[5] found that  $\text{DO}_3$  domains nucleated in both the  $\alpha$  and B2 matrices in the size range of 150 to 250 Å after annealing at 450 °C. The equilibrium thermodynamics predicts a weak variation in between the rate of growth of  $\text{DO}_3$  LRO and B2 LRO. Fultz[34] found that the growth of B2 LRO and  $\text{DO}_3$  LRO differs to a great extent because of different temperature sensitivity of growth rate of those two ordered phases. Therefore, Fultz concluded that the observed behavior must have a kinetic origin, since equilibrium thermodynamics predicts the opposite trend.

Over a wide composition range (23-55 at% Al), high concentration of non-equilibrium defects, vacancies and anti-site defects can be hosted in the Fe-Al binary alloy system, without decreasing consistently the degree of long range order. One of

the reasons of this be relies in the particularly low energies of vacancy formation,  $E_F$ . The net activation energy,  $E_A$ , can be divided into two parts. i.e.

$$E_A = E_F + E_M \quad \dots \quad 2.6$$

Where,  $E_M$  = vacancy migration energy.

In the  $DO_3$  phase and B2 phase of Fe-Al alloys, low values of  $E_A$  were measured [figure-2.14] and that would be mainly due to very low value of  $E_F$ [35]. Thus in Fe-Al system, increase of the activation energy of the ordering process is not observed. This effect is probably due to the role played by the vibrational properties in enhancing the atomic mobility.

## **2.5: APPLICATION OF IRON ALUMINIDES**

Iron Aluminides compete with 300 and 400 series stainless steels and some nickel based alloys. Specific advantages includes: (1) Excellent sulfidation resistance, (2) oxidation resistance, (3) lower density, (4) good wear resistance, (5) cavitation-erosion resistance and potentially lower cost. Based on these advantages, several applications have been identified for the  $Fe_3Al$  based alloys which include the following:

1. **Sintered Porous Gas Metal Filters:** In this application, the filters are used to remove particulate matter from the gas produced in the coal gassification process and the other processes where the gas contains the higher sulfur content. Advantage is taken of the superior sulfidation resistance of iron aluminide alloys as opposed to any other currently available material. The filters are prepared by sintering powders to a desired level of porosity
2. **Heating Elements:** This application uses the iron aluminide alloy wire for heating elements in toasters, ovens and dryers. Advantage is taken of the high resistivity, which remain constant up to 1000 °C, and the excellent oxidation resistance. The fabrication of wire has been hampered by limited ductility at room temperature. However, the hot-rolled bar is currently feasible as furnace heating elements.
3. **Furnace Fixtures:** This application takes advantage of the excellent oxidation resistance of iron-aluminide alloys for components such as retorts, rollers, beams,

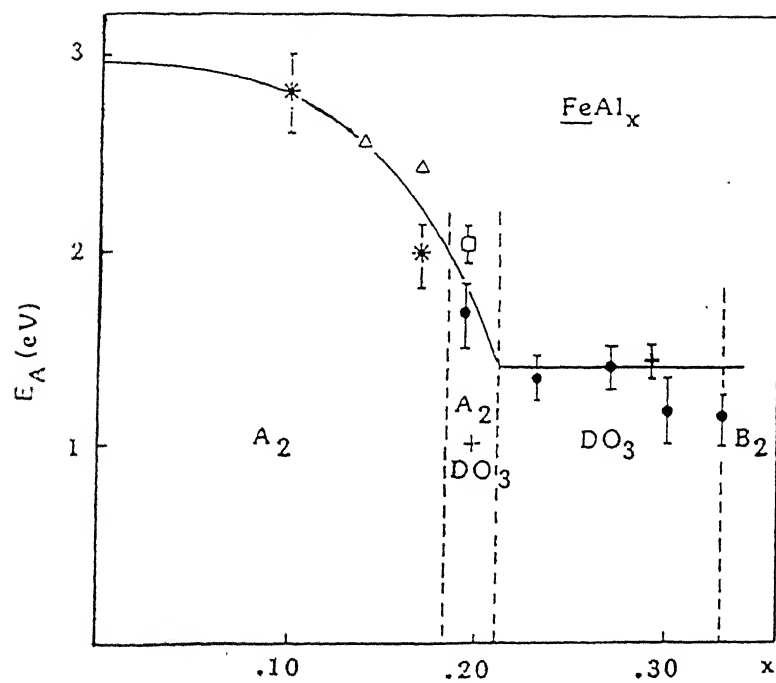


Figure-2.14: Activation energies versus  $x$  in  $\text{Fe}_{1-x}\text{Al}_x$  [35]

etc. The furnace fixtures are expected to be manufactured by various casting processes.

4. **Catalytic Converter Substrate:** This application takes advantage of the excellent oxidation resistance of iron aluminides. The 0.050 mm thick foil for this application is prepared primarily by warm rolling followed by cold rolling in the last few passes.
5. **Regenerator Disks:** In this application, iron aluminides is used as a heat exchanger in a gas turbine engine. Advantage is taken of the excellent oxidation and sulfidation resistance. The foil requirements for this application are similar to those for the catalytic converter substrates.
6. **Component For Molten Salt Applications:** Iron aluminide alloys have excellent compatibility with oxidizing and carbonate salts. Processes dealing with molten salts have the potential of using iron aluminides for their containment, transfer or even rotating components. The components for this application will be manufactured by a combination of the casting process, hot working ingots and welding.
7. **Shielding:** This application uses iron aluminide as a shielding to prevent the excessive oxidation of tubes in power plants and incinerators. The shields are typically 3 to 4 mm thick and are shaped like tubes. These shields are typically manufactured by bending the warm rolled sheet of the desired thickness.

## EXPERIMENTAL PROCEDURE

As mentioned in the chapter-1, aim of this work is to study the effect of heavy deformation and air cooling on the phase transformation. The starting rolled strips, on which transmission electron microscopic study is done, are obtained in the finished form. Therefore, procedure followed in TEM observation will be started after a brief history of the starting material.

### **3.1: MATERIAL**

The starting material is obtained in the cast form, from Defence Metallurgical Research Laboratory (DMRL) Hyderabad. The composition of the material is Fe-28 at% Al. The alloy ingot supplied by the DMRL is thermomechanically treated by A. Agarwal[36] and S. Suwas[37] Cast ingot is annealed at 1000 °C for 4 hours to minimize segregation.

In the present study, thermomechanical treatment to the alloy is guided by the equilibrium diagram. The above mentioned homogenized material is cut into 10 mm thick from the ingot, soaked in the furnace for 1 hour and rolled at the following three temperatures.

1. 500 °C (ordered DO<sub>3</sub> phase)
2. 800 °C (ordered B2 phase)
3. 1000 °C (disordered  $\alpha$  phase)

All the blocks are rolled down to 1.5 mm thick strip. Thus the materials obtained after such processing, are used for their microstructural examination in the present study.

### **3.2: THIN FOIL PREPARATION**

Preparation of thin foils from the rolled strip is done in two stages. Firstly, samples are subjected to primary thinning which is done manually and then secondary thinning is done by Electrojet polishing.

The rolled strips are thin enough to go directly for primary thinning by emery paper. Starting thinning is done by grinding on the emery paper number 2. Surface smoothening is done by grinding on the emery paper number 4 and then on emery paper number 6. Thus the foils obtained from three different rolled strips are having the thickness in the range of 0.6 mm to 0.8 mm, with minimum macroscopic irregularities. These foils are punched by a hand punch into 3 mm diameter disks.

Electrojet polishing of 3 mm. diameter disks samples is done by a automatic dual jet polisher, Menupol-2, supplied by Struers Company. The circuit diagram of the dual jet polisher is shown in the figure-3.1. The composition of the electrolyte is 1000 ml ethanol(99.9% purity) and 15 ml perchloric acid (60.0% concentrated).

Before the disks are subjected to jet thinning they are degreased by acetone. The low temperature of the electrolyte is maintained at  $-30^{\circ}\text{C}$  using liquid nitrogen. The voltage of the electrolyte cell is set at 20 volts and the corresponding cell current observed is  $\sim 10$  m amps. The perforation of the foils is detected automatically, after which the flow of the electrolyte is stopped. After completion of the thinning, samples are washed with methyl alcohol to remove electrolyte from its surface, dried up and kept inside a desiccator.

### **3.3: MICROSTRUCTURAL ANALYSIS BY THE TRANSMISSION ELECTRON MICROSCOPY:**

The electron diffraction pattern obtained by transmitted electron beam depends largely on crystal size of the diffracting medium and limiting aperture used. Number of stages should be carefully performed to obtain a good diffraction pattern from a selected area of the specimen. These steps are as follows.

- Object plane of the intermediate lens should coincide with the plane of aperture. This is done by controlling the intermediate lens current to focus the selector aperture on the screen.
- Specimen image should be coplanar with the selector aperture. This is done by adjusting objective lens current.

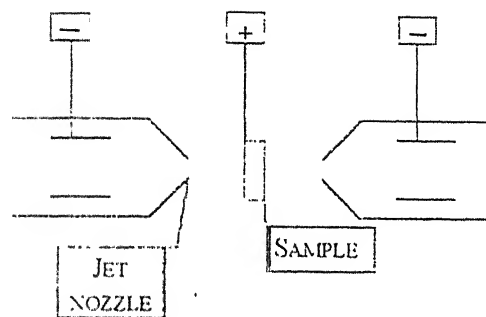


Figure-3.1: Schematic diagram of a dual jet polisher.

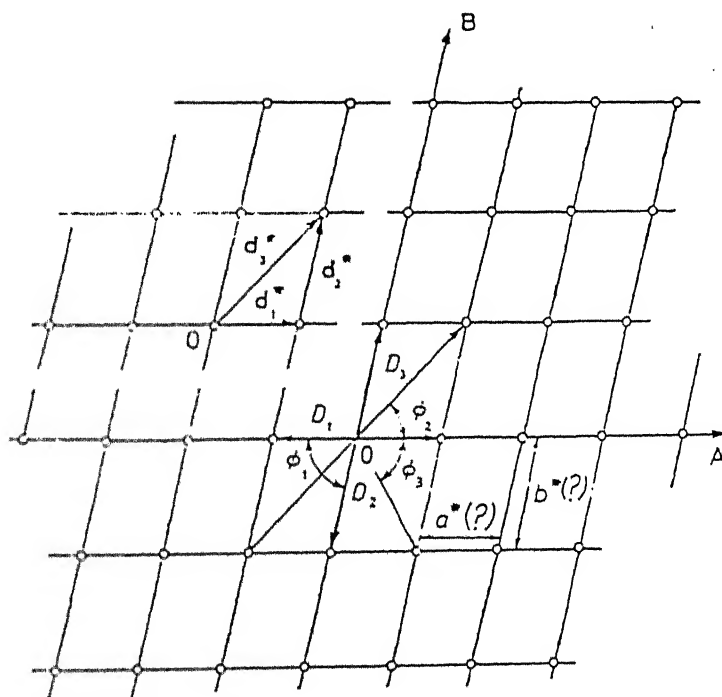


Figure-3.2: Diagrammatic representation of a spot pattern. (Possible reciprocal cell edges along OA and OB.)[30]

- The diffraction image from the back focal plane of the objective lens can be imaged by decreasing the intermediate lens current to 'diffracting position'. A fine adjustment to the lens current to have a minimum spot size.
- The parallel beam of electrons illuminate the specimen. This is done by controlling the condenser lens current.

When viewed properly a single crystal can give rise to spot pattern in TEM. Each spot in the pattern is related to a certain plane in the crystal. Solving the pattern, identification of the selected area via crystal structure can be obtained.

The spot pattern of unbroken sequence must satisfy the zone equation. If  $[uvw]$  denotes the direction of the zone axis, all points which lie on the diffraction pattern near center must satisfy the following zone equation.

$$hu + kv + lw = 0 \quad \dots \quad 3.1$$

where  $(hkl)$  denotes plane via spot on the pattern.

Analysis of patterns was done by measuring

- The distances of the spot from the central spot 'O' i.e.  $R_1, R_2, R_3$ , from which corresponding 'd' spacings of the planes are calculated (figure-3.2) [30].
- The angles such as  $\Phi_1, \Phi_2, \Phi_3$ , etc. between the reciprocal vectors and hence between the planes, giving rise to the diffraction spots which subtend these angles at 'O' (figure-3.2).

Interplaner spacing 'd' was calculated from the relationship

$$d = L\lambda/R \quad \dots \quad 3.2$$

Where,

$L$  = Camera Length.

$\lambda$  = Wavelength of the electron beam used.

Anticipating that certain phases are involved to give rise the pattern under consideration, it is possible, from the measured values of the d's and  $\Phi$ 's to predict. The phase can be confirmed by comparison of measured and standard d-spacing and the calculated and measured interplanar angles. Thus, when two planes say,  $(h_1k_1l_1)$  and  $(h_2k_2l_2)$  are identified, the zone axis can be obtained from the following relation:



$$u = k_1 l_2 - k_2 l_1 \quad \dots \quad 3.3(a)$$

$$v = l_1 h_2 - l_2 h_1 \quad \dots \quad 3.3(b)$$

$$w = h_1 k_2 - h_2 k_1 \quad \dots \quad 3.3(c)$$

The indexing of the other spots are done by vector addition formula i.e.

$$R_3 = R_2 + R_1 \quad (3.4)$$

If  $R_1$  stands for  $(h_1 k_1 l_1)$ ,  $R_2$   $(h_2 k_2 l_2)$  and  $R_3$  for  $(h_3 k_3 l_3)$  then following the above relation we can write,

$$h_3 = h_2 + h_1 \quad \dots \quad 3.5(a)$$

$$k_3 = k_2 + k_1 \quad \dots \quad 3.5(b)$$

$$l_3 = l_2 + l_1 \quad \dots \quad 3.5(c)$$

The points near the central spot are chosen to form a parallelogram. The distances from the central spot ( $R$ -values) are measured and with the help of camera constant  $d$ -spacing are found. From the symmetry of the diffraction pattern and ratio of the distances of the two spots, zone axis and planes are anticipated. The spots, which are equidistant from the center and diametrically opposite are associated with the same set of crystal planes and are indexed  $hkl$  and  $\bar{h} \bar{k} \bar{l}$ . Indexing is checked by comparing the measured  $\Phi$ -values and calculated  $\Phi$  values. Once the  $d$ -values are found out the lattice parameter can be found out by the following relationship:

$$1/d^2 = (h^2 + k^2 + l^2)/a^2 \quad \dots \quad 3.6$$

$$a = d\sqrt{(h^2 + k^2 + l^2)} \quad \dots \quad 3.7$$

The patterns are magnified While developing from the negatives. Therefore, actual distance ' $R$ ' in the reciprocal lattice is obtained after dividing the distance, measured from the photograph, by the positive to negative magnification (mentioned as 'pos. to neg.' in the tables of chapter-4) factor. For analysis, the diffraction patterns are copied on a plane paper by means of tracing paper. The angles, written by the side of the patterns compares the angles measured from the patterns with the theoretically calculated values. The possible zones and the phases, responsible for the corresponding reciprocal lattices are written thereby.

In this study, few photographs are taken by Phillips Transmission Electron Microscope operated at 100 kV at Indira Gandhi Center for Atomic Research, Kalpakkam as well as at IIT, Madras and rest of the photographs were taken by JEOL, JEM-2000FX, operated at 160 kV.

## RESULTS AND DISCUSSION

In this chapter the micrographs and diffraction patterns of the rolled samples, obtained from TEM, are presented. The samples rolled at 1000 °C are abbreviated as RS1000. Similarly, samples rolled at 800 °C and the samples rolled at 500 °C are denoted as RS800 and RS500 respectively. In this thesis photographs of figure-4.1 to 4.26 are obtained from RS1000, figure-4.27 to 4.35 are obtained from RS800 and figure-4.36 to 4.42 are obtained from RS500.

The wavelength of the electron beam is function of the accelerating voltage of the electron gun. The table-4.1 gives wavelength of the electron beam at various accelerating voltages. Table 4.2 to 4.4 gives the x-ray diffraction data of powders of Fe-25 at% Al ( $\text{DO}_3$ ),  $\alpha$ -iron and FeAl (B2) materials respectively. These data are used for analyzing the diffraction patterns in the present study.

In this study, analysis of diffraction patterns is presented in the following way. The reciprocal lattice shown in the figure-4.3(a) is the schematic representation of the figure-4.3. The analysis of a particular pattern is given in the corresponding table-4.3(a). As for example, the distances of the points 'A', 'B' and 'C', measured from the figure-4.3(a) are 6.25 mm, 7.5 mm and 9.5 mm respectively. The distances of the corresponding spots on the negative, which was nothing but the true 'R' in the table-4.3(a), are 2.08 mm, 2.5 mm and 3.167 mm respectively. Knowing the camera length,  $L = 150$  mm and wavelength of the electron beam,  $\lambda = 0.0284$  Å (from table-4.1), camera constant found to be 4.26 mm-Å. This camera constant is written at the beginning of the table-4.3(a). The 'd' spacing corresponding to each spot is obtained from the equation-3.2. So the calculated d-spacings of 'A' 'B' and 'C' are 2.048 Å, 1.704 Å and 1.345 Å respectively. Comparing these calculated values with the standard data from the "Powder Diffraction File"[38,39], planes corresponding to each spots are predicted. Therefore the spot 'A' indicates  $(02 \bar{2})$ , spot 'B' indicates  $(311)$ , and spot 'C' indicates  $(33 \bar{1})$  planes of  $\text{DO}_3$ . The indexed pattern is confirmed by



Figure-4.1: RS1000



Figure-4.2: RS1000

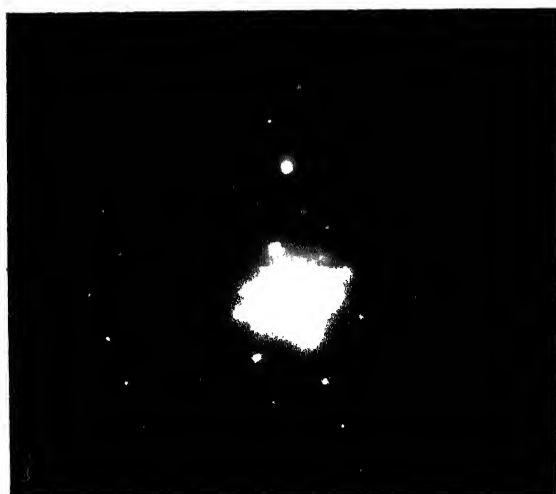


Figure-4.3: RS1000



Figure-4.4: RS1000

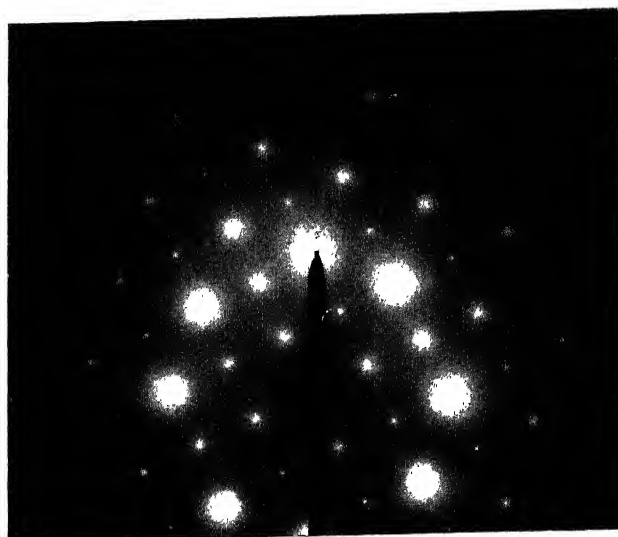


Figure-4.5: RS1000

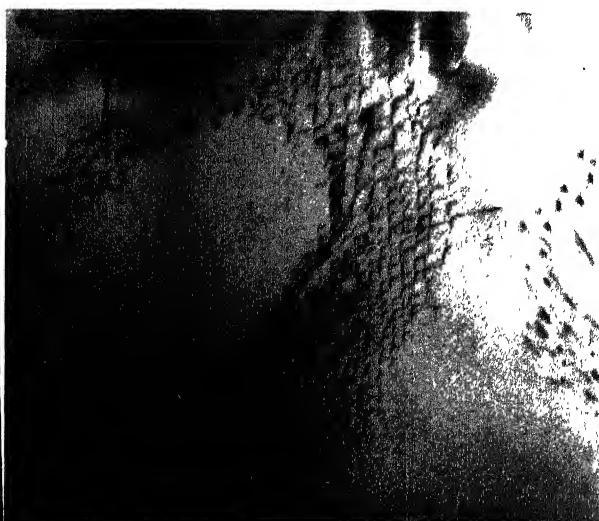


Figure-4.6: RS1000

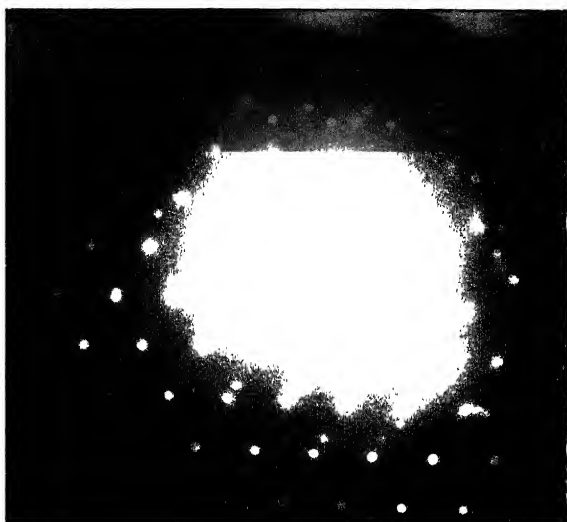


Figure-4.7: RS1000

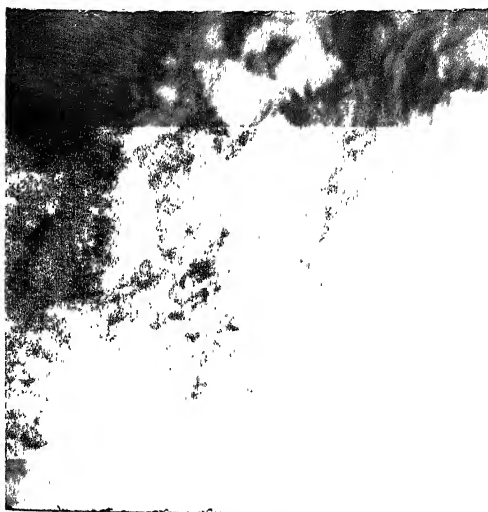


Figure-4.8: RS1000



Figure-4.9: RS1000

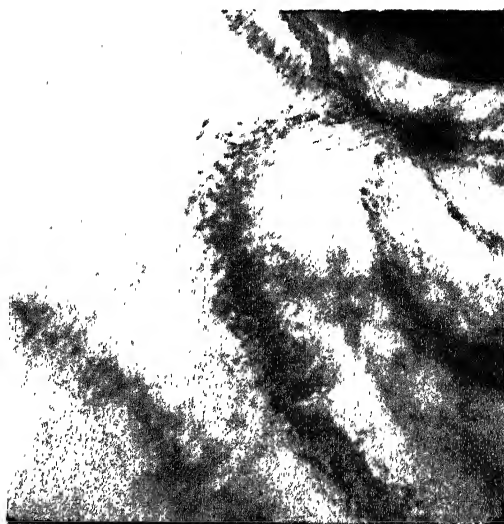


Figure-4.10: RS1000

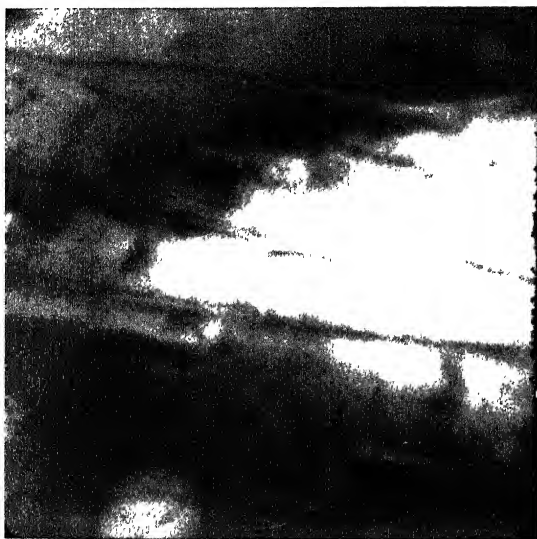


Figure-4.11: RS1000

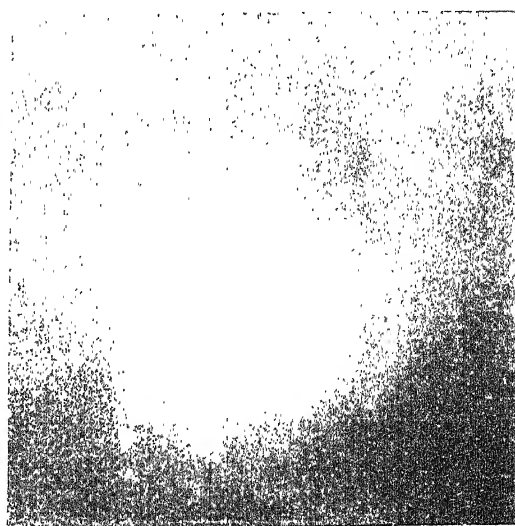


Figure-4.12: RS1000

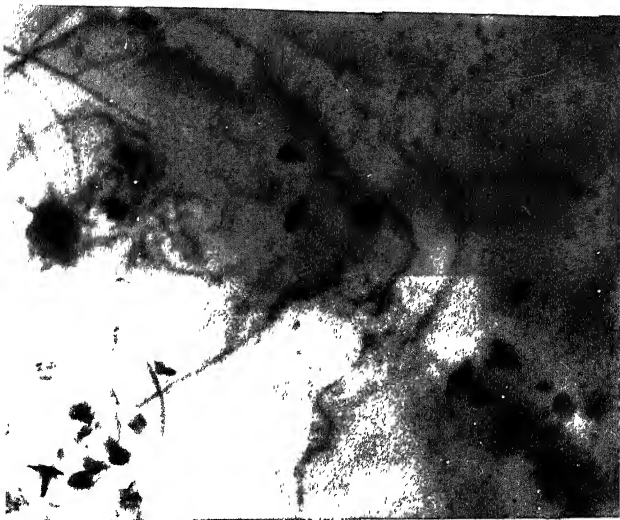


Figure-4.13: RS1000

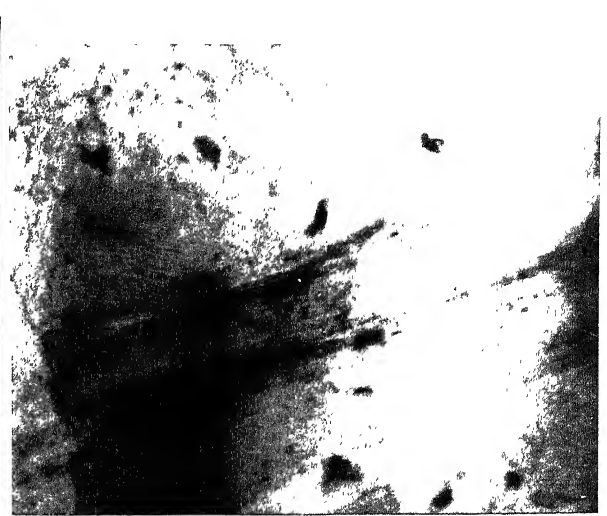


Figure-4.14: RS1000

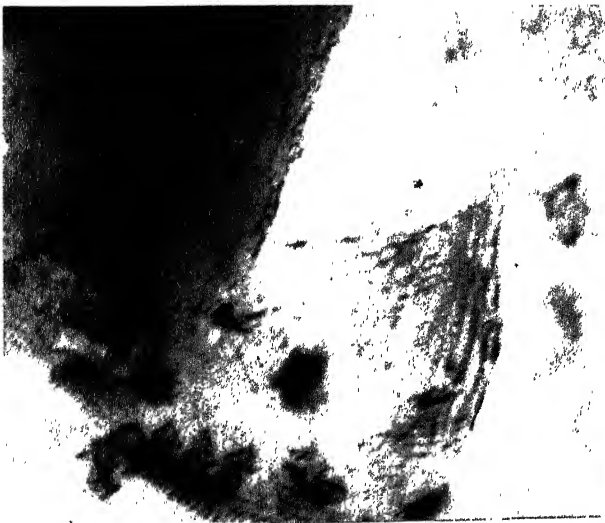


Figure-4.15: RS1000

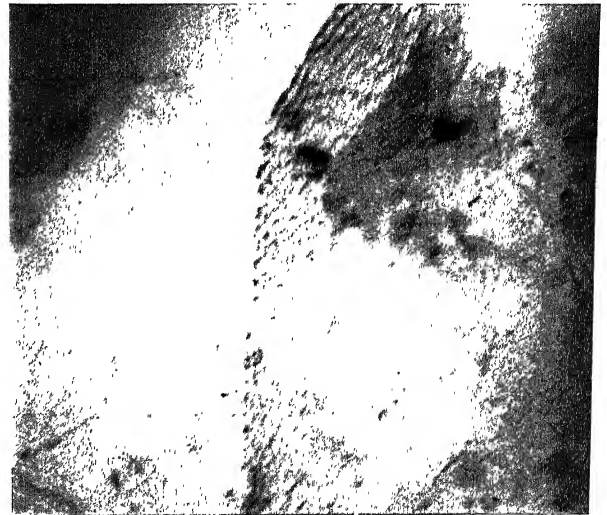


Figure-4.16: RS1000

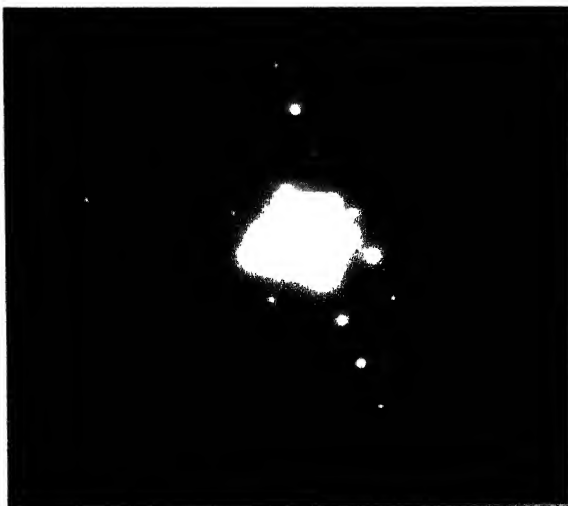


Figure-4.17: RS1000



Figure-4.18: RS1000

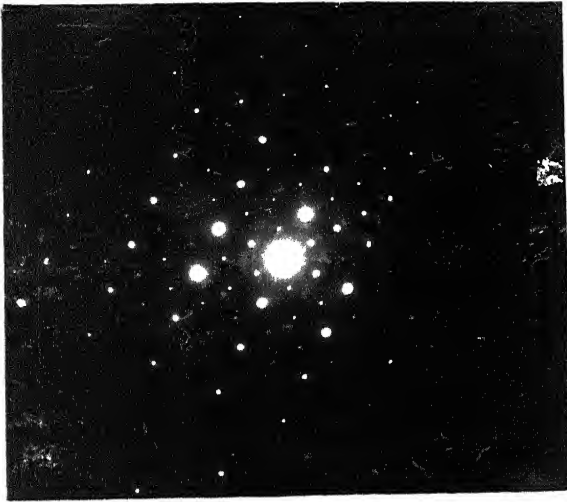


Figure-4.19: RS1000



Figure-4.20: RS1000

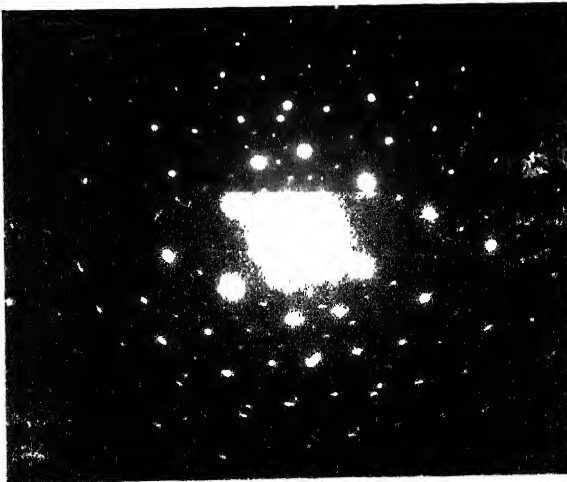


Figure-4.21: RS1000



Figure-4.22: RS1000



Figure-4.23: RS1000



Figure-4.24: RS1000



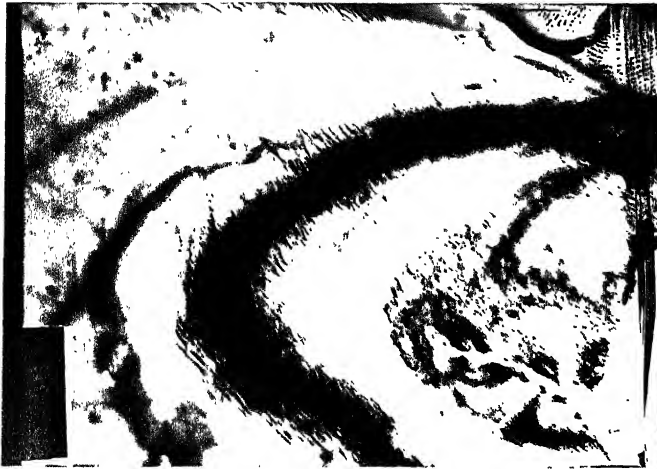


Figure-4.25: RS1000



Figure-4.26: RS1000



Figure-4.27: RS800



Figure-4.28: RS800

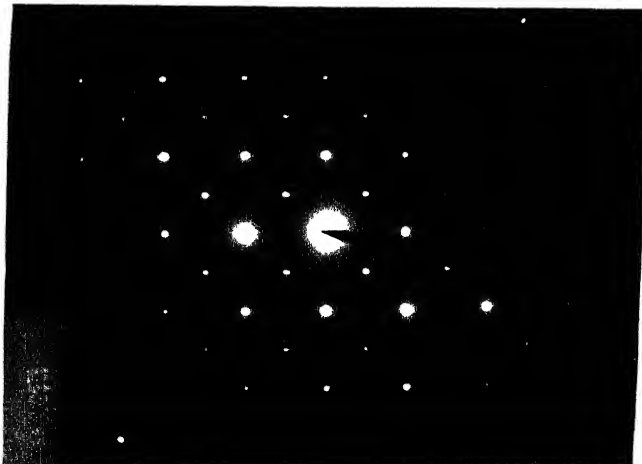


Figure-4.29: RS800



Figure-4.30: RS800



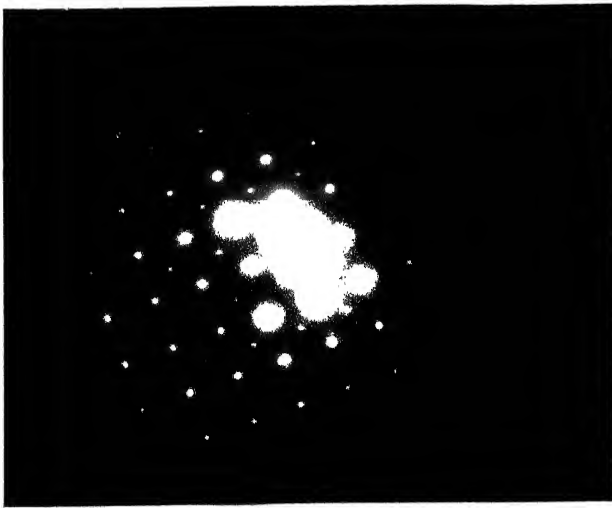


Figure-4.31: RS800



Figure-4.32: RS800

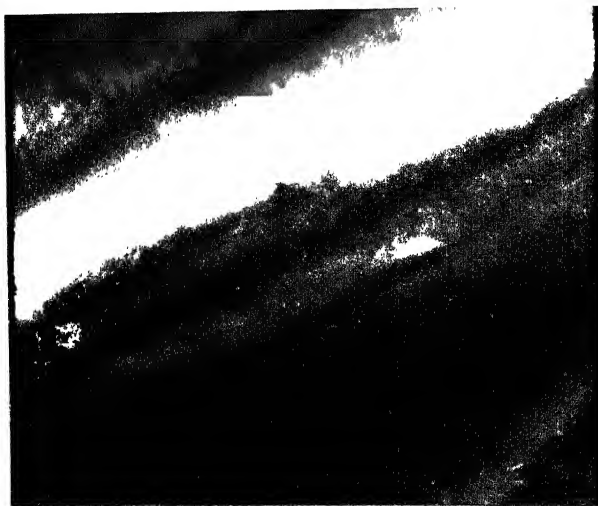


Figure-4.33: RS800

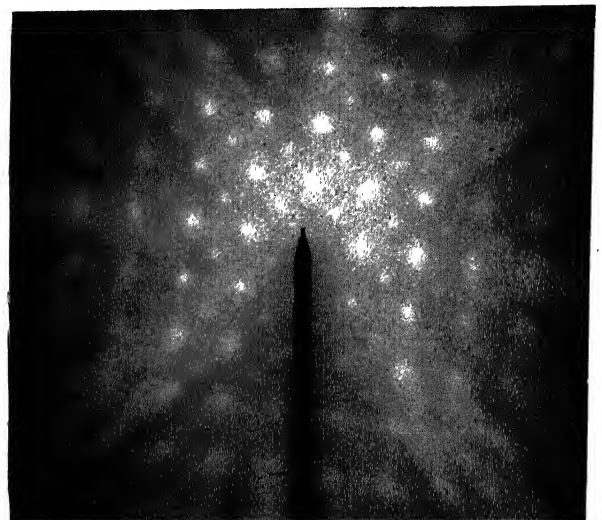


Figure-4.34: RS800

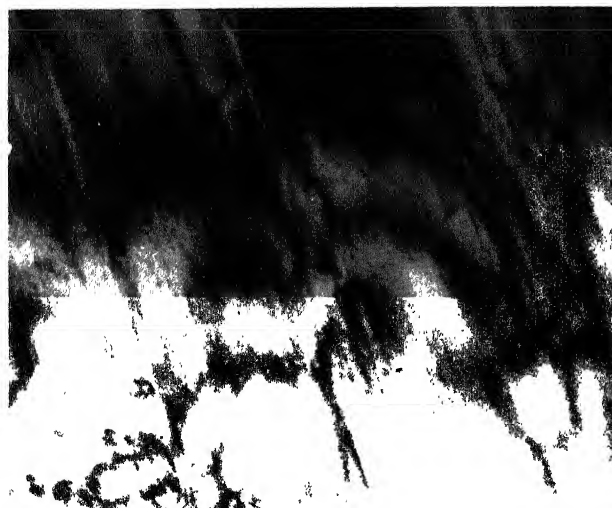


Figure-4.35: RS800



Figure-4.36: RS500

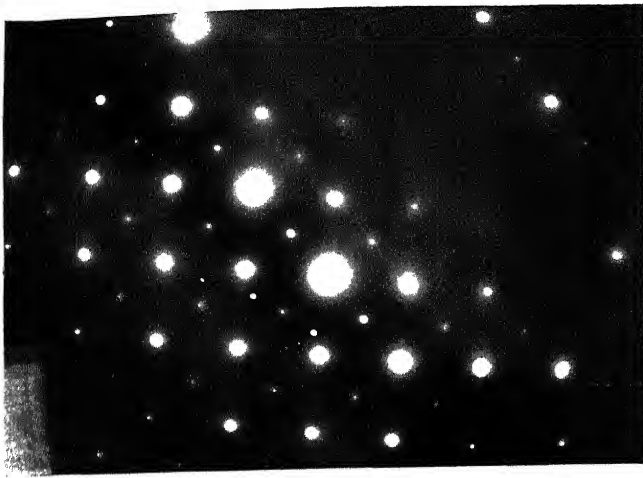


Figure-4.37: RS500

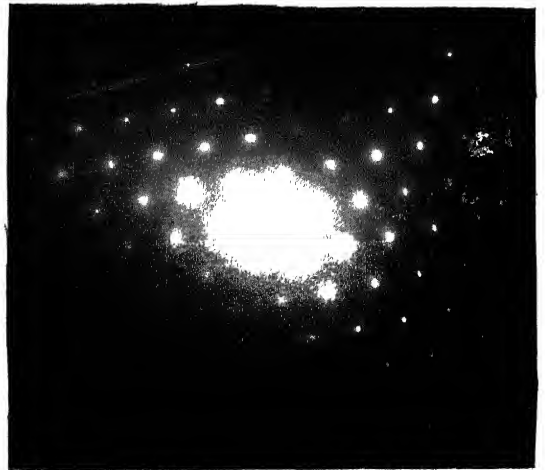


Figure-4.38: RS500



Figure-4.39: RS500

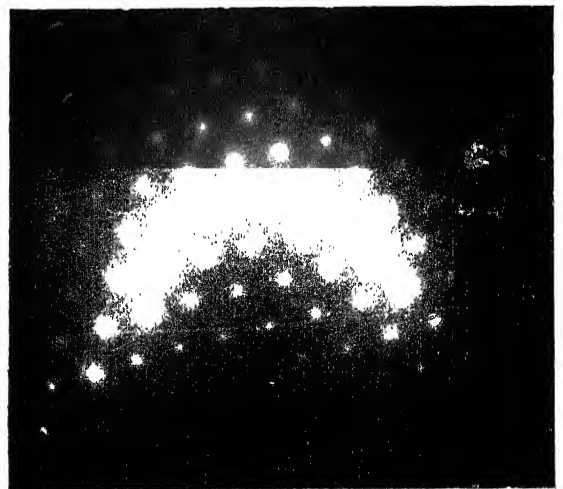


Figure-4.40: RS500



Figure-4.41: RS500

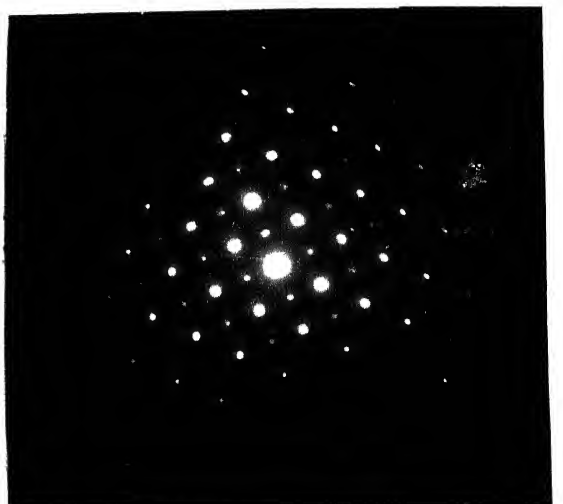


Figure-4.42: RS500

4

kV	80	100	120	160
$\lambda, \text{\AA}$	0.0418	0.0370	0.0337	0.0284

TABLE-4.2

X-ray diffraction data of  $\text{Fe}_3\text{Al}(\text{DO}_3)$  [39].

d	2.04	1.45	1.34	3.34	(Fe <sub>8</sub> Al) <sub>16</sub> C			
I/I <sub>1</sub>	100	80	60	60	IRON ALUMINUM			
Rad. Peak	λ 1.9373	Pulver	d Å	I/I <sub>1</sub>	hkl	d Å	I/I <sub>1</sub>	hkl
Dist.	Out off	Coll	3.34	60	111			
I/I <sub>1</sub> Visual		d corr. about	2.89	50	200			
Rad. Bradley and Jay, Proc. Roy. Soc., London, 1934		2.04	100	220				
		1.79	20	311				
		1.67	10	222				
Syn. Cubic		S.G. Fm $\bar{3}m$ (225)	1.45	80	400			
a = 3.78	b =	c =	A	C	331			
α	β	γ	Z 4	1.33	10	420		
Rad. 1st ord.				1.29	10	422		
				1.18	90	511, 333		
				1.11	20	440		
1st	2nd	3rd	4th	5th	6th	7th	8th	9th
2V	D	mp	Color					
Rad.								
Under 200 $\times$ type								

X-ray diffraction data of  $\alpha$ (disordered b.c.c.) iron [39].

d	2.03	1.17	1.43	2.03	(Fe)28					
I/I <sub>1</sub>	100	30	20	100	IRON (α PHASE)					
					IRON (KAMACITE)					
Rad. CuKα	1.5405	Filter Ni	d Å	I/I <sub>1</sub>	hkl	d Å	I/I <sub>1</sub>	hkl		
Dis. Cutoff		Coll.	2.0268	100	110					
I/I <sub>1</sub> COUNTER DIFFRACTOMETER	d corr. adm.7		1.4332	20	200					
Ref. SHANNON ET AL., 1958 CIRCULAR 539, Vol. II, P. 3			1.1702	30	211					
			1.0134	10	220					
			0.9044	12	310					
Sym. Cubic		S.G. Im3m (229)								
a = 2.8664 Å	c	A	C							
b	Y	Z 2	.8273	6	222					
Ref. Ibid.										
1 Å	2Y	D7.874 mp	Color	Sign						
Ref. Ibid.										
TOTAL IMPURITIES OF SAMPLE 40.0013% EACH METALS AND NON-METALS.										
X-RAY PATTERN AT 25°C. X-RAY STRUCTURE TYPE.										
OCCURS AS TERRESTRIAL "IRON" AND IN METEORITES AS "KAMACITE".										

TABLE-4.4

X-ray diffraction data of FeAl(B2) [38].

AlFe	d Å	Int	hkl	d Å	Int	hkl
Aluminum Iron	2.899	8	100			
	2.048	100	110			
	1.6722	3	111			
	1.4472	14	200			
	1.2949	2	210			
	1.1820	25	211			
	1.0238	8	220			
	0.9650	1	300			
	0.9157	9	310			
	0.8358	4	222			
Rad. CuK $\alpha_1$ 1.5405 Å Filter Mono. d-sp Diff.						
Coll. Latt. Diffractometer V <sub>low</sub> (21)						
Ref. Nat. Bur. Stand. (U.S.) Monogr. 25, 185 (1981)						
Sym. Cubic S.G. Fm3m (221)						
a = 2.8954(2) Å b c A C						
Ref. Ibid. Y Z 1 mp						
D <sub>5</sub> 5.605 D <sub>m</sub> SS/FOM F <sub>10</sub> = 54(.0169,11)						
Color Dark gray Pattern at 25°C The sample was obtained from the Metallurgy Section of the National Bureau of Standards, CAS#: 12042-17-0. It had been heated to 800°C for 5 days and cooled to room temperature in 4 days. CsCl 11pc. Tungsten used as internal standard. PSC: cP2. To replace 1-1257.						

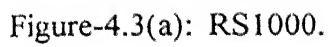
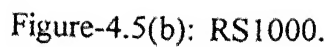


TABLE-4.3(b)

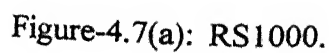
[illegible]

**TABLE-4.5(b)**

Figure-4.5(a): RS1000.



$\{h_1 k_1 l_1\}$	$\{h_2 k_2 l_2\}$	Measured $\phi$	Theoretical $\phi$
100	110	44.0	45.0
100	010	46.0	45.0



$\{h_1 k_1 l_1\}$	$\{h_2 k_2 l_2\}$	Measured $\phi$	Theoretical $\phi$
202	220	62.5	60.0
202	02 $\bar{2}$	120.0	120.0



Figure-4.9(a): RS1000.

TABLE-4.9(b)

$\{h_1 k_1 l_1\}$	$\{h_2 k_2 l_2\}$	Measured $\phi$	Theoretical $\phi$
02 2	420	71.0	71.57
402	420	38.0	39.23

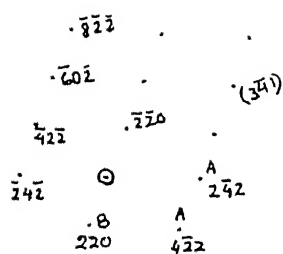


Figure-4.12(a):RS1000.

TABLE-4.12(b)

$\{h_1 k_1 l_1\}$	$\{h_2 k_2 l_2\}$	Measured $\phi$	Theoretical $\phi$
24 2	42 2	34.0	33.56
24 2	220	71.0	73.22
24 2	60 2	60.0	58.91

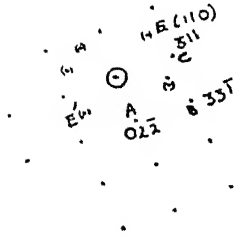


Figure-4.17(a):RS1000.

TABLE-4.17(b)

$\{h_1 k_1 l_1\}$	$\{h_2 k_2 l_2\}$	Measured $\phi$	Theoretical $\phi$
311	33 1	40.0	40.46
311	02 2	89.0	90.0

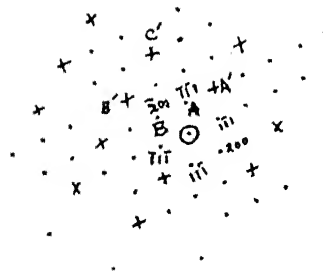


Figure-4.19(a):RS1000.

TABLE-4.19(b)

$\{h_1 k_1 l_1\}$	$\{h_2 k_2 l_2\}$	Measured $\phi$	Theoretical $\phi$
11 1	200	56.0	54.74
11 1	11 1	70.5	70.52
200	21 1	35.0	35.26
200	01 1	89.0	90.0



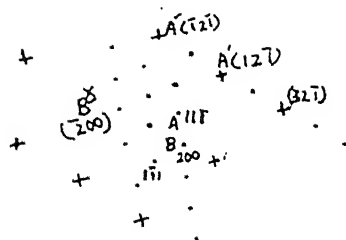


Figure-4.21(a):RS1000.

TABLE-4.21(b)

$\{h_1 k_1 l_1\}$	$\{h_2 k_2 l_2\}$	Measured $\phi$	Theoretical $\phi$
11 1	200	55.0	54.74
11 1	11 1	68.5	70.52
200	12 1	64.0	65.91

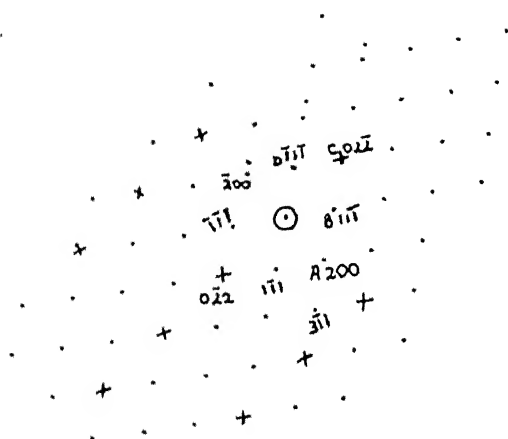


TABLE-4.26(b)

$\{h_1 k_1 l_1\}$	$\{h_2 k_2 l_2\}$	Measured $\phi$	Theoretical $\phi$
200	11 1	56.0	54.74
200	02 2	90.0	90.0

Figure-4.26(a):RS1000.

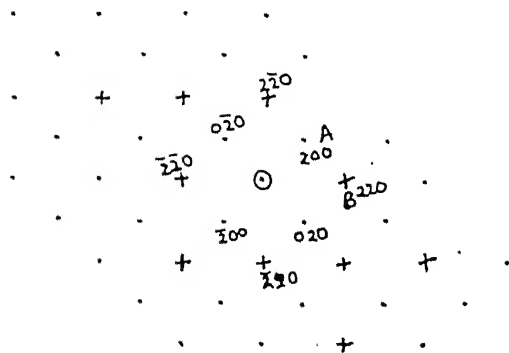


Figure-4.29(a):RS800.

TABLE-4.29(b)

$\{h_1k_1l_1\}$	$\{h_2k_2l_2\}$	Measured $\phi$	Theoretical $\phi$
200	220	44.0	45.0
200	0 20	90.0	90.0

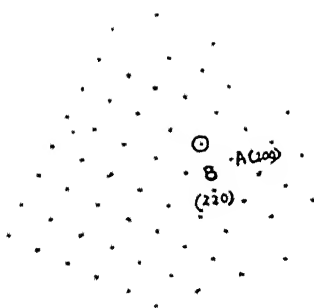


Figure-4.31(a):RS800.

TABLE-4.31(b)

$\{h_1k_1l_1\}$	$\{h_2k_2l_2\}$	Measured $\phi$	Theoretical $\phi$
200	220	44.5	45.0
200	0 20	89.0	90.0

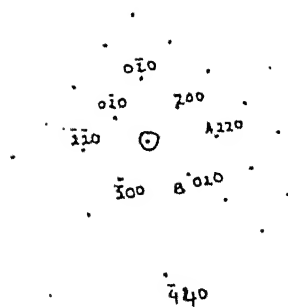


Figure-4.34(a):RS800.

TABLE-4.34(b)

$\{h_1k_1l_1\}$	$\{h_2k_2l_2\}$	Measured $\phi$	Theoretical $\phi$
200	220	44.0	45.0
200	0 20	90.0	90.0

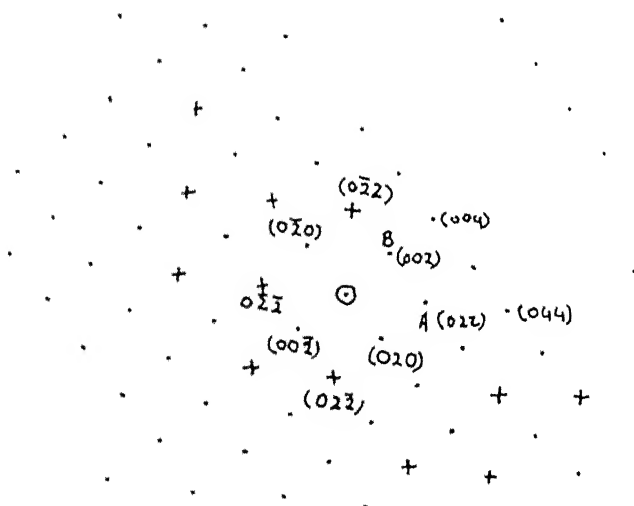


Figure-4.37(a):RS500.

TABLE-4.37(b)

$\{h_1k_1l_1\}$	$\{h_2k_2l_2\}$	Measured $\phi$	Theoretical $\phi$
200	220	44.5	45.0
200	0 20	90.5	90.0



Figure-4.38(a):RS500.

TABLE-4.38(b)

$\{h_1k_1l_1\}$	$\{h_2k_2l_2\}$	Measured $\phi$	Theoretical $\phi$
202	220	58.5	60.0
200	0 22	61.0	60.0

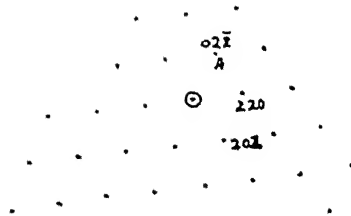


Figure-4.40(a):RS500.

TABLE-4.40(b)

$\{h_1k_1l_1\}$	$\{h_2k_2l_2\}$	Measured $\phi$	Theoretical $\phi$
202	220	60.5	60.0
200	0 22	61.0	60.0

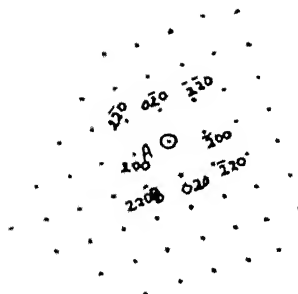


Figure-4.42(a):RS500.

TABLE-4.42(b)

$\{h_1k_1l_1\}$	$\{h_2k_2l_2\}$	Measured $\phi$	Theoretical $\phi$
200	220	44.5	45.0
200	020	46.0	45.0

TABLE-4.3(a)

RS1000; L=150 mm, 160 kV,  $L\lambda=4.26 \text{ mm-}\text{\AA}$ 

R(IN FROM FIGURE	MM)	NEG. POS. MAG.	TO	TRUE 'R'(IN MM)	'd' SPACING (IN $\text{\AA}$ ) CALCULATE D	STANDARD	{hkl}
A 6.25				2.08	2.048	2.04	02 $\bar{2}$ DO <sub>3</sub>
B 7.5		3.0		2.5	1.704	1.79	311 DO <sub>3</sub>
C 9.5				3.167	1.345	1.33	33 $\bar{1}$ DO <sub>3</sub>

TABLE-4.5(a)

RS1000; L= 230 mm, 100 kV,  $L\lambda=8.51 \text{ mm-}\text{\AA}$ 

R(IN FROM FIGURE	MM)	NEG. POS. MAG.	TO	TRUE 'R'(IN MM)	'd' SPACING (IN $\text{\AA}$ ) CALCULATE D	STANDARD	{hkl}
A 8.75		3.0625		2.857	2.978	2.89	200 DO <sub>3</sub> 100 B2
B 12.25				4.00	2.127	2.04	220 DO <sub>3</sub> 110 B2

TABLE-4.7(a)

RS1000; L=155 mm, 100 kV,  $L\lambda=5.735 \text{ mm-}\text{\AA}$ 

R(IN FROM FIGURE	MM)	NEG. POS. MAG.	TO	TRUE 'R'(IN MM)	'd' SPACING (IN $\text{\AA}$ ) CALCULATE D	STANDARD	{hkl}
A 8.25		3.0625		2.69	2.13	2.048	220 DO <sub>3</sub> 110 B2
B 8.25				2.69	2.13	2.048	220 DO <sub>3</sub> 110 B2

TABLE-4.9(a)

RS1000; L=150 mm, 160 kV,  $L\lambda=4.26 \text{ mm-}\text{\AA}$ 

R(IN FROM FIGURE	MM)	NEG. POS. MAG.	TO	TRUE 'R'(IN MM)	'd' SPACING (IN $\text{\AA}$ ) CALCULATE D	STANDARD	{hkl}
A 6.5		3.0		2.16	1.972	2.04	220 DO <sub>3</sub>
B 10				3.3	1.28	1.29	420 DO <sub>3</sub>

TABLE-4.12(a)

RS1000; L=150 mm, 160 kV,  $L\lambda=4.26$  mm-Å

R(IN FROM FIGURE	MM)	NEG. POS. MAG.	TO	TRUE 'R'(IN MM)	'd' SPACING CALCULATE D	(IN Å) STANDARD	{hkl}
A 6.5		3.0		2.16	1.972	2.04	220 DO <sub>3</sub> 110 B2
B 11.5				3.83	1.12	1.18	422 DO <sub>3</sub> 211 B2

TABLE-4.17(a)

RS1000; L=150 mm, 160 kV,  $L\lambda=4.26$  mm-Å

R(IN FROM FIGURE	MM)	NEG. POS. MAG.	TO	TRUE 'R'(IN MM)	'd' SPACING CALCULATE D	(IN Å) STANDARD	{hkl}
A 4.26				2.08	2.048	2.04	02 $\bar{2}$ DO <sub>3</sub>
B 9.5				3.167	1.345	1.33	33 $\bar{1}$ DO <sub>3</sub>
C 7.5		3.0		2.5	1.704	1.79	311 DO <sub>3</sub>
E 6.25				2.08	2.048	2.04	011 $\alpha$
E' 6.25				2.08	2.048	2.04	011 $\alpha$

TABLE-4.19(a)

RS1000; L=150 mm, 160 kV,  $L\lambda=4.26$  mm-Å

R(IN FROM FIGURE	MM)	NEG. POS. MAG.	TO	TRUE 'R'(IN MM)	'd' SPACING CALCULATE D	(IN Å) STANDARD	{hkl}
A 4.0				1.33	3.20	3.34	111 DO <sub>3</sub>
B 4.6				1.53	2.78	2.89	200 DO <sub>3</sub>
A' 6.5		3.0		2.16	1.972	2.04	110 $\alpha$
B' 9.5				3.16	1.34	1.44	200 $\alpha$
C' 11.25				3.75	1.136	1.182	211 $\alpha$

TABLE-4.21(a)

RS1000; L=150 mm, 160 kV,  $L\lambda=4.26$  mm-Å

R(IN FROM FIGURE	MM)	NEG. POS. MAG.	TO	TRUE 'R'(IN MM)	'd' SPACING CALCULATE D	(IN Å) STANDARD	{hkl}
A 4.0				1.33	3.20	3.34	111 DO <sub>3</sub>
B 4.6		3.0		1.53	2.78	2.89	200 DO <sub>3</sub>
A' 11.5				3.833	1.11	1.18	211 B2
B' 9.0				3.0	1.42	1.43	200 B2

TABLE-4.26(a)

RS1000; L=575 mm, 100 kV,  $L\lambda=21.275$  mm-Å

R(IN FROM FIGURE	MM)	NEG. POS. MAG.	TO	TRUE 'R'(IN MM)	'd' SPACING CALCULATE D	(IN Å) STANDARD	{hkl}
B 6.0				6.0	3.5	3.34	11 $\bar{1}$ DO <sub>3</sub>
A 7.5		1		7.5	2.84	2.89	200 DO <sub>3</sub>
C 10.0				10.0	2.1	2.04	02 $\bar{2}$ DO <sub>3</sub>

TABLE-4.29(a)

RS800; L=575 mm, 100 kV,  $L\lambda=21.275$  mm-Å

R(IN FROM FIGURE	MM)	NEG. POS. MAG.	TO	TRUE 'R'(IN MM)	'd' SPACING CALCULATE D	(IN Å) STANDARD	{hkl}
A 7.5		1		7.5	2.84	2.89	200 DO <sub>3</sub>
B 10.0				10.0	2.1	2.04	02 $\bar{2}$ DO <sub>3</sub>

TABLE-4.31(a)

RS800; L=150 mm, 160 kV,  $L\lambda=4.26$  mm-Å

R(IN FROM FIGURE	MM)	NEG. POS. MAG.	TO	TRUE 'R'(IN MM)	'd' SPACING CALCULATE D	(IN Å) STANDARD	{hkl}
A 4.25		2.875		1.478	2.88	2.89	200 DO <sub>3</sub> 100 B2
B 6.0				2.087	2.04	2.04	220 DO <sub>3</sub> 110 B2

TABLE-4.34(a)

RS800; L=155 mm, 100 kV,  $L\lambda=5.735$  mm-Å

R(IN FROM FIGURE	MM)	NEG. POS. MAG.	TO	TRUE 'R'(IN MM)	'd' SPACING CALCULATE D	(IN Å) STANDARD	{hkl}
A 8.5		3.06		2.78	2.06	2.04	220 DO <sub>3</sub> 110 B2
B 6.0				1.96	2.92	2.89	200 DO <sub>3</sub> 100 B2

TABLE-4.37(a)

RS500; L=575 mm, 100 kV,  $L\lambda=21.275$  mm-Å

R(IN FROM FIGURE	MM)	NEG. POS. MAG.	TO	TRUE 'R'(IN MM)	'd' SPACING CALCULATE D	(IN Å) STANDARD	{hkl}
B 7.5		1		7.5	2.84	2.89	200 DO <sub>3</sub>
A 10.0				10.0	2.1	2.04	02 $\bar{2}$ DO <sub>3</sub>

TABLE-4.38(a)

RS500; L=150 mm, 160 kV,  $L\lambda=4.26$  mm-Å

R(IN FROM FIGURE	MM)	NEG. POS. MAG.	TO	TRUE 'R'(IN MM)	'd' SPACING CALCULATE D	(IN Å) STANDARD	{hkl}
A 6.0		2.85		2.105	2.028	2.04	220 DO <sub>3</sub> 110 B2

TABLE-4.40(a)

RS500; L=150 mm, 160 kV,  $L\lambda=4.26$  mm-Å

R(IN FROM FIGURE	MM)	NEG. POS. MAG.	TO	TRUE 'R'(IN MM)	'd' SPACING CALCULATE D	(IN Å) STANDARD	{hkl}
A 6.0		2.85		2.105	2.028	2.04	220 DO <sub>3</sub> 110 B2

TABLE-4.42(a)

RS500; L=150 mm, 160 kV,  $L\lambda=4.26$  mm-Å

R(IN FROM FIGURE	MM)	NEG. POS. MAG.	TO	TRUE 'R'(IN MM)	'd' SPACING CALCULATE D	(IN Å) STANDARD	{hkl}
A 4.5		2.85		1.57	2.71	2.89	200 DO <sub>3</sub> 100 B2
B 6.0				2.105	2.028	2.04	220 DO <sub>3</sub> 110 B2



comparing the angles subtended at the center by the spots 'A', 'B' and 'C' with the theoretical values of their angles [see table-4.3(b), given with the figure 4.3(a)]. All other diffraction patterns are analyzed and presented in the same manner.

As discussed in chapter-3, after indexing the pattern and cross checking them by measuring the angles subtended at the center by the spots, zone axis is obtained in the following way. If  $(\bar{1}11)$  and  $(200)$  is considered then with the help of the relations mentioned in the equations-3.3 following things can be written,

$$u = k_1l_2 - k_2l_1 = 0$$

$$v = l_1h_2 - l_2h_1 = \bar{2}$$

$$w = h_1k_2 - h_2k_1 = \bar{2}$$

which can be reduced to  $[0\ \bar{1}\ \bar{1}]$  and is same as  $[011]$ .

Spot patterns belonging to  $[001]$ ,  $[111]$  and  $[113]$  types of zones, obtained from B2 and  $\text{DO}_3$  are similar. However, the intensity of a particular spot would vary from B2 to  $\text{DO}_3$ . As for example, the figure-4.5 could be identified as a pattern resulting from either B2 or  $\text{DO}_3$ , having  $[001]$  zone axis. The nearest spot 'A' could be identified as  $(100)$  of B2 or  $(200)$  of  $\text{DO}_3$ . Therefore, the pattern of figure-4.5 are indexed, after  $\text{DO}_3$  in the figure-4.5(a) and after B2 in the figure-4.5(b). The x-ray data of table-4.4 gives the intensity corresponding to  $(100)$  of B2 to be 8% of the maximum intensity (corresponding to  $(110)$  spot). For the same d-value, the x-ray data of table-4.2 predicts the intensity of the  $(200)$  spot to be 50% of the maximum intensity (corresponding to  $(220)$  spot of  $\text{DO}_3$ ). It can be assumed that increase in at% of Al in B2 increase the  $(100)$  spot intensity resulting from B2, as  $(100)$  spot can not be expected from  $\alpha$ -phase (table-4.3). The material under examination contains 28 at% Al, which predicts even more weaker intensity from  $\{100\}$  type of spots in comparison to the  $(100)$  spot intensity mentioned in the table-4.4. The patterns of  $[001]$ ,  $[111]$  and  $[113]$  zones, obtained in this study are having significant spot intensities and therefore predicted as the case where an ordering intermediate to B2 and  $\text{DO}_3$  has occurred. This phenomena is similar to the observation of Oki et al[40]. In all the above cases, spots are denoted after the planes of  $\text{DO}_3$  phase but the planes of B2 phase, corresponding to each spot can be obtained after dividing the  $\{hkl\}$  of  $\text{DO}_3$  by a factor

of 2 and therefore mentioned in the corresponding tables. As for example, instead of  $\{220\}$  of  $\text{DO}_3$ ,  $\{110\}$  of B2 or instead of  $\{422\}$  of  $\text{DO}_3$ ,  $\{211\}$  of B2 can be read. Therefore, the figure-4.6 is indexed twice, as in figure-4.5(a) and figure-4.5(b) where figure-4.5(a) is indexed after  $\text{DO}_3$  and figure-4.5(b) is indexed after B2.

Samples rolled at 1000 °C to 80% deformation showed considerable degree of  $\text{DO}_3$  ordering. Figure-4.1 shows the arrangement of superdislocations in the APB, which can be compared with Chen et al[31] Morris et al[32] (figure-2.11). In the present study figure 4.4, 4.6, 4.8, 4.11, 4.13, 4.15, 4.16, 4.23, 4.24 show either perfect or imperfect variants of superdislocations. Existence of strain enables the ordinary dislocations to exist in the lattice, as pointed out by Chen et al[31] and can be observed in figure-2.10(a), (b) and (c). In this study figure-4.2, 4.10, 4.20 and 4.25 show regions where little or no recovery has taken place and can be compared with figure-2.10(c). When analyzed, figure 4.3 and 4.17 indicate the existence of  $\text{DO}_3$  in the samples rolled at 1000 °C. These patterns are resulted from the regions where two different phases are existing. The predominant pattern is caused by the  $\text{DO}_3$  superstructure with a zone axis of  $[\bar{2}33]$ . The spots like E and E', [see figure-4.3(a)] which are (111) type and which are about to form a ring near center, indicates the existence of fine B2 domains. B2  $\{111\}$  reflection being weak in nature, they appear in the pattern as faint spots. Here an orientation relationship between B2 and  $\text{DO}_3$  can be established, i.e.

$$[\bar{2}33] \text{DO}_3 \parallel [\bar{1}11] \text{B2}$$

Figure-4.4 shows morphology of moving dislocations. The negative of the photograph has observed a magnification of  $\frac{1}{4}$  th of what is written in that figure. But while developing the photographs it was magnified by 3 times. So this photograph is actually showing features at  $75,000 \times$  magnification. Near the tip of the dark band dislocations are roughly separated by a distance of 7.5 mm. This indicates that in the rolled strip they are separated by a distance of around 1000 Å. If this is compared with the figure-2.6, a 0.3 to 0.45 degree of ordering can be expected.

The streaks, connecting the spots in the pattern of figure-4.5 is the indication of strained lattice, where recovery has taken place to a less extent. In this figure very

bright, doubly diffracted spots are observed. They indicate suitably oriented, coexistence of two phases in that selected area. The diffraction pattern (figure-4.7) obtained from the APB fault shows spots, which have arisen from the doubly twinned structure. Thus it confirms that area is an APB. This can again be confirmed with figures of 2.12. The dislocation arrangement in the recovery state is well explained by J. P. Hirth[33]. Magnified view of dislocation arrangement can be seen in the figure-2.13(a). Here local relaxation of boundary dislocation has occurred after reaction with an oblique lattice dislocation. Solid lines before and dashed lines after relaxation. Hirth pointed out that, before relaxation it is the situation where a  $\frac{1}{2}[111]$  dislocation in molybdenum is entering a  $\frac{1}{2}[1\bar{1}\bar{1}]$  tilt wall and represented by the firm line. This situation is very similar to that of Fe-28 at% Al, as mentioned by D. G. Morris, where the prior deformation substructure has recovered to a well defined subgrain structure without achieving recrystallization. He pointed out that the APB was composed of  $\frac{1}{2}\langle 100 \rangle$  type dislocations and resulted by the reaction between the dissociated  $\frac{1}{4}\langle 111 \rangle$  dislocations produced during deformation. Such subgrain walls are strong barriers to further deformation, since the  $\frac{1}{2}\langle 100 \rangle$  are not having suitable slip planes to move at room temperature. At the same time this subgrain walls do not constitute interfaces where fracture can easily nucleate. Therefore this type of structure leads to high hardness without the loss of ductility.

The selected area diffraction (SAD) pattern (figure-4.9) obtained from the region of figure-4.8, which is obtained from RS1000, indicates  $\text{DO}_3$  ordered structure having  $[\bar{1}22]$  zone axis and can be compared with figure-2.12(a). Micrograph of  $\text{DO}_3$  superlattice dislocation is shown in the figure-4.11 and SAD pattern from that region is shown in the figure-4.12. The dislocation in the figure-4.11 is having a spacing of about 1300 Å, when compared with the result of Stoloff et. al.[4] (figure-2.6), it indicates an ordering of approximately  $S=0.4$ . Figure-4.13 to 4.16 shows the subgrain boundary formation, similar to that of figure-4.6 and 4.8, at various regions. Figure-4.17 is similar to that of figure 4.3 but here the multiple spots of  $\{110\}$  types are more prominent. The spots which are about to form a ring near the center, is caused by the small domains of  $\alpha$ , from that region. The prominent reciprocal lattice is resulted from  $\text{DO}_3$  ordered structure having a  $[\bar{2}33]$  zone axis.

The spots in the figure-4.19, obtained from the region of figure-4.2, are resulted from the single phase region but the pattern can be separately indexed as if they are resulted either from  $\text{DO}_3$  or B2 having  $[011]$  zone axis. As (200) of B2 is similar to (400) of  $\text{DO}_3$  higher intensities are resulted in those regions. Therefore, it can be conceived that, an intermediate stage of ordering between  $\text{DO}_3$  and B2 can exist and has occurred in the present case. The pattern from that region is given in the figure-4.20. Similar is the case of figure-4.21, where the zone of the separate spot patterns is not exactly the same. The closely placed spots are indication of  $\text{DO}_3$  phase in the RS1000.

Figure-4.23 shows some foreign particles which have become needle shaped because of rolling. Next figure[figure-4.24] depicts one such particle at high magnification. The dislocations around the particles are also observed, which can lead to high hardness in the material. No cracks were found at the interface. Because of thickness and small size, no diffraction pattern was obtained from such particle.

Figure-4.27 is obtained from the RS800. The heavily dislocated region indicates that no recovery has occurred in that area, whereas in figure-4.28 superlattice dislocations are observed having low dislocation density. In most of the cases, as it is evident from the figures-4.27, 4.30, 4.32 and 4.33 recovery of the strained structure is poor. Appearance of relatively intense spots at  $\{100\}$  B2/ $\{200\}$   $\text{DO}_3$  positions indicate an ordering intermediate to B2 and  $\text{DO}_3$ . Because of high degree of deformation and poor recovery, the ordinary dislocations, those caused deformation at high temperature exist at room temperature. Therefore, no perfect superlattice dislocation can be seen in RS800 and RS500. The SAD patterns of figure-4.29, 4.31 and 4.34 and SAD patterns of figure-4.37, 4.38, 4.40 and 4.42 of RS500 can either be indexed after  $\text{DO}_3$  or B2. Patterns of figure-4.29, 4.31, 4.34, 4.37 and 4.42 are resulted from  $\langle 001 \rangle$  types of zones whereas, figure-4.38 and 4.40 are resulted from  $\langle 111 \rangle$  types of zone. As mentioned earlier, in this type of zones both B2 and  $\text{DO}_3$  result same type of spot patterns. In both the RS500 and RS800, a spot pattern, spread over a large area are observed. If spots are of nearly equal intensity in such situation they indicate presence

very large. Diffraction from higher indices planes of B2 are very weak. Therefore, they are unlikely to be detected in the patterns obtained from the low Al content [Fe-28 at% Al] B2 structure. As all the patterns from RS800 and RS500 are having large number of spots, resulted from higher indices planes, they indicate formation of DO<sub>3</sub> in those samples.

Following the reports of Fultz[34] and Vennégués and Cadeville[35], as given in the section-2.4, it is obvious that, large amount of non-equilibrium vacancies are formed en route to heavy deformation and fast cooling, forced the structure to be guided mainly by kinetics. It is already mentioned that in the DO<sub>3</sub> phase and B2 phase of Fe-Al alloys, low values of  $E_A$  are measured (figure-2.14) and that would be mainly due to very low values of  $E_F$  (vacancy formation energy)[35]. When thin rolled strips are air cooled, it observed a fast cooling. Therefore, the samples, rolled at 1000 °C are having a lot of vacancies at room temperature. It is also known that the order-disorder transformation in this alloy system is diffusion controlled second order transformation. Therefore, at low temperature where DO<sub>3</sub> is thermodynamically stable, it is formed by diffusion mechanism, assisted by the vacancies. The formation and availability of vacancies are greatly influenced by the temperature as it is an exponential function of temperature. So, the ordering achieved in the RS1000 is more prominent than those of RS800 and RS500. Thus, in the present study heavy deformation and fast cooling forced the structure to be guided by kinetics mainly and has resulted a certain degree of DO<sub>3</sub> ordering.

## CONCLUSION

Effect of thermomechanical treatment has a great influence in the ordering process of Iron-Aluminides and is established with the help of TEM. The lattice parameters of  $\alpha$ , B2 and  $\text{DO}_3$  are closely related and are based on the same crystal structure. The superlattice reflection from the ordered phase, obtained in the selected area diffraction pattern makes the characterization of the phases easy.

At certain zones, similar type of spot patterns can arise from both the B2 and  $\text{DO}_3$  ordered structure. It is found out that intensity of the spots from the higher indices planes are almost absent in case of B2. The spot patterns, having significant intensity indicates presence of  $\text{DO}_3$  in this structure. From the measured dislocation spacing it is concluded that degree of ordering achieved is in the range of 0.3 to 0.45. There is supposed to exist an orientation relationship between the parent and product phase and this is predicted from the doubly diffracted spot intensities.

The ordering is more prominent in samples rolled at 1000 °C rather than the samples rolled at 800 °C and 500 °C. The reason of this phenomena is attributed to the low values of vacancy formation and is supported by the report from the other research workers.

## REFERENCES

1. M. G. Mendiratta, S. K. Ehlers and H. A. Lipsitt, *Metall. Trans.*, **18A**, (1987) 509.
2. H. P. Longworth and D. Z. Mikkola, *Mat. Sci. Eng.*, **91** (1987) 213.
3. C. G. Mckamey and J. A. Horton, *Metall. Trans.*, **20A**, (1989) 751.
4. N. S. Stoloff and R. G. Davis, *Acta Metall.*, **12**, (1964) 473.
5. K. Oki, M. Hasaka and T. Eguchi, *Japan J. Appl. Phys.*, **12**, (1973) 1522.
6. C. T. Liu, E. H. Lee and C. G. Mckamey, *Scr. Metall. Mater.*, **25**, (1989) 875.
7. R. J. Lynch, L. A. Heldt and W. W. Milligan, *Scr. Metall. Mater.*, **25**, (1991) 2147.
8. L. Guttman, *Solid State Phys.* **3**, (1956) 188.
9. O. Kubaschewski, *Iron-Binary Phase Diagram*, Springer-Verlag Berlin Heidelberg, Germany, p.6.
10. S. M. Allen and J. W. Cahn, *Acta Metall.*, **24**, (1976) 425.
11. P. R. Swann, W. R. Duff and R. M. Fisher, *Metall. Trans.*, **3**, (1972) 409.
12. L. Anthony and B. Fultz, *Acta Metall. Mater.*, **43**, (1995) 3885.
13. M. Yamaguchi, D. P. Pope V. Vitek and Y. Umakoshi, *Phil. Mag. A*, **43**, (1981) 1265.
14. M. Yamaguchi and Y. Umakoshi, *Progress. in Materials Science*, **34**, (1990) 20.
15. A. Ball and R. E. Smallman, *Acta Metall.*, **14**, (1966) 1517.
16. R. C. Crawford and I. L. F. Ray, *Phil. Mag.*, **35**, (1977) 549.
17. M. G. Mendiratta, H. M. Kim and H. A. Lipsitt, *Metall. Trans.*, **15A**, (1984) 65.
18. C. Engelke and H. Neuhäuser, *Scr. Metall.*, **33**, (1995) 1109.
19. S. Hanada, S. watanabe, T. Sato and O. Izumi, *Scr. Metall.*, **15**, (1981)1345.
20. M. Yamaguchi and Y. Umakoshi, *Progress in Materials Science*, **34**, (1990) 115.
21. A. R. Causey and E. Teghtsoonian, *Metall. Trans.*, **1**, (1970) 1177.
22. R. T. Fortum and D. E. Mikkola, *Mater. Sci. Eng.*, **91**, (1987) 223.
23. C. G. Mckamey, J. A. Horton and C. T. Liu, *MRS Symp. Proc.*, High Temperature Ordered Intermetallic Alloys-II, eds. N. S. Stoloff, C. C. Koch, C. T. Liu and O. Izumi, MRS, Pittsburgh, (1987) p.231.
24. M. A. Morris and D. G. Morris, *Acta Metall.* **38**, (1990) 551.

25. M. Yamaguchi and Y. Umakoshi, *Progress in Materials Science*, **34**, (1990) 135.
26. W. Yan, *Scr. Metall.*, **21**, (1991) 1511.
27. M. Rudy and G. Sauthoff, *Mater. Sci. Eng.*, **81**, (1986) 525.
28. C. G. Mckamey, C. T. Liu, S. A. David, J. A. Horton and J. V. Cathcart, *Fossil Energy Mat. Prog. Conf. Proc.*, ORNL/FMP-87/4, (1987) p.683.
29. H. C. Jung, C. R. Park, C. S. Lee and C. G. Park, *TMS Symp. Proc.*, "Processing properties and Application of Iron Aluminides", eds. J. H. Schneibel and M. A. Crimp, TMS, Pennsylvania, (1994) 171.
30. "Interpretation of Electron Diffraction Pattern", K. W. Andrews (1971) 28.
31. G. Chen, Y. Huang, W. Yang and Z. Sun, *TMS Symp. Proc.*, "Processing properties and Application of Iron Aluminides", eds. J. H. Schneibel and M. A. Crimp, TMS, Pennsylvania, (1994) 171.
32. D. G. Morris and M. Leboeuf, *Acta Metall. Mater.*, **42**, (1994) 1817.
33. J. P. Hirth, *Metall. Trans.*, **3**, (1972) 3047.
34. B. Fultz, "Ordering and Disordering in Alloys", *Proc. European Workshop*, ed. A. R. Yavari, (1991) 31-42.
35. P. Vennégues, M. C. Cadeville, V. Pierron-Bohnes and F. Afyouni, *Acta Metall. Mater.*, **38**, (1990) 2199.
36. A. Agarwal, M.Tech Thesis, MME, IIT, Kanpur, (1995), 25.
37. S. Suwas, M.Tech Thesis, MME, IIT, Kanpur, (1994), 20.
38. JCPDS, *International Centre for Diffraction Data*, **33**, (1989) 7.
39. *Joint Committee on Powder Diffraction Standards*, **6**, (1967) 150.
40. K. Oki, H. Sagane and T. Eguchi, *Japan J. Appl. Phys.*, **13**, (1974) 753.
41. K. Sumino, *Sci. Rep. Res. Inst., Tohoku Univ.* **A10**, (1959) 283.



**A 124444**

## Date Slip

This book is to be returned on the  
date last stamped. 124444

MME-1986-M-BHA-SOM.